A targeting black phosphorus nanoparticle based immune cells nano-regulator for photodynamic/photothermal and photo-immunotherapy

Xiaoge Zhang, Junjie Tang, Chao Li, Yao Lu, Lili Cheng, Jie Liu*

School of Biomedical Engineering, Sun Yat-sen University, Guangzhou, Guangdong 510006, China

ABSTRACT

Photo-immunotherapy is a novel therapeutic approach against malignant tumors with minimal invasiveness. Herein, a targeting multifunctional black phosphorus (BP) nanoparticle, modified by PEGylated hyaluronic acid (HA), was designed for photothermal/photodynamic/photo-immunotherapy. *In vitro* and in *vivo* assays indicated that HA-BP nanoparticles possess excellent biocompatibility, stability, and sufficient therapeutic efficacy in the combined therapy of photothermal therapy (PTT) and photodynamic therapy (PDT) for cancer therapy. Moreover, the results of *in vitro* showed that HA-BP down-regulated the expression of CD206 (M2 macrophage marker) by 42.3% and up-regulated the ratio of CD86 (M1 macrophage marker) by 59.6%, indicating that HA-BP nanoparticles have functions in remodeling tumor associated macrophages (TAMs) phenotype (from pro-tumor M2 TAMs to anti-tumor M1 macrophages). Fluorescence (FL) and photoacoustic (PA) multimodal imaging confirmed the selective accumulation of HA-BP in tumor site via both CD44$^+$ mediated active targeting and passive EPR effect. *In vitro* and in *vivo* studies suggested that the combined therapy of PDT, PTT and immunotherapy using HA-BP could not only significantly inhibit original tumor but also induce immunogenic cell death (ICD) and release Damage-associated molecular patterns (DAMPs), which could induce maturation of dendritic cells (DCs) and activate effector cells that robustly evoke the antitumor immune responses for cancer treatment. This study expands the biomedical application of BP nanoparticles and displays the potential of modified BP as a multifunctional therapeutic platform for the future cancer therapy.

1. Introduction

In present clinical practices, traditional cancer treatment strategies including chemotherapy, surgery and radiotherapy have various limitations such as invasiveness, limited treatment efficiency, inevitable toxic effects caused by the lack of tumor specific targeting and risk of tumor recurrence [1–3]. Hence, it is necessary to exploit original nanomaterials and advanced methods for cancer treatment. Phototherapy, including PTT and PDT mediated by nanomaterials, has aroused considerable interest with its advantages such as low systemic cytotoxicity, high spatiotemporal selectivity, non-invasiveness and minimal trauma [4,5]. For phototherapy, photosensitizers (PS) or photothermal agents (PTA) absorb the energy of incident light and produce reactive oxygen species (ROS) or local heating to cause tumor cells apoptosis [6–9]. The combined therapy of PDT and PTT is a desirable therapeutic method, because PDT could disturb tumor physiology by interfering with tumor microenvironment (TME) to increase the sensitively of tumor cells to PTT [10]. Meantime, heat produced by PTT can increase blood flow and

thus improve oxygen supply to enhance the therapeutic outcomes of PDT [11]. In addition, the tumor cell debris produced by phototherapy could act as tumor-associate antigens and cause anti-tumor immune responds to eliminate residual and metastatic cancer cells [12,13]. However, the effect of phototherapy is severely influenced by the tissues penetration depth of NIR light, and anti-tumor immune effect induced by phototherapy is not enough to alleviate the immunosuppression of tumor microenvironment [14]. Therefore, a combination of photo-immunotherapy and modulation of the TME could be a desirable strategy to improve the anti-tumor effect.

Among various PDT and PTT agents, black phosphorus (BP) as a notionally two-dimensional (2D) layered inorganic material has been widely used as nano agents for tumor therapy due to its excellent electrical conductivity, optical properties and low toxicity [15–18]. In particular, BP with ultra-small sizes gained more attention due to its higher photothermal conversion efficiency and faster clearance [19]. However, the application of ultra-small BP is limited due to several inherent drawbacks such as instability and poor targeting capability

[20]. To improve the stability and tumor specificity of BP nanoparticles, various modified and functionalized systems of BP nanosheets or quantum dots with polymer [21,22], biomolecules [23] and inorganic nanoparticles [24–26] are designed to stabilize BP and broaden the possibilities for its applications. So in comparison with previous work, we are aiming to develop the surface modified BP nanoparticle with size around 50 nm, which might be more stable and easier for tumor accumulation than both ultra-small BP quantum dots or large size nanosheets [27,28].

Tumor associated macrophages (TAMs) make up crucial components of TME and majorly present in tumor hypoxic regions [29,30]. Nominally, there are two main subtypes of macrophages *in vivo*, classically activated macrophages (M1) and alternatively activated macrophages (M2) [30]. M1 macrophages release the pro-inflammatory cytokines (such as interleukin-6 [IL-6], IL-12, IL-23 and tumor necrosis factor [TNF]), reactive nitrogen and oxygen species (such as NO, H_2O_2, iNOS and superoxide), resulting in an antitumor effect [31,32]. In contrast, M2 macrophages release pro-tumor cytokines (IL-4, IL-10, IL-13, growth factors, matrix metalloproteinase-9 [MMP-9] and so on) in tumor microenvironment, to promote tumor progression and metastasis [33]. Hence, coinstantaneous re-regulating macrophage subtype (from pro-tumor M2 to antitumor M1) can be an efficient strategy for tumor immunotherapy [34–36]. To re-educate pro-tumor M2 TAMs to antitumor M1 macrophages, many mediators such as ferumoxytol [34], histone deacetylase inhibitors [36] and chloroquine [37] are used to improve anti-tumor efficiency. As a polysaccharide, HA has been applied diffusely for the advanced drug and gene delivery systems because of its biocompatibility, biodegradability, non-immunogenicity, and tumor targeting specificity ($CD44^+$ receptor) [38,39]. Besides, it has proved that HA with different molecular weights could serve as an important immunoregulator to promote different inflammatory factors and signals, low molecular weight HA (MW < 5 kDa) can induce the conversion of TAMs into M1 macrophages, while high molecular weight HA (> 800 kDa) can promote the conversion of TAMs into M2 macrophages [40,41]. In addition, Chen et al. [42] have proved that low molecular weight HA modified nanoparticles can reverse TAMs from M2 into M1 macrophages to improve the tumor therapeutic efficiency.

In this study, low molecules weight HA was used to modify BP nanoparticles to improve the stability and targeting specificity of BP as well as remodel the phenotype of TAMs. As shown in Scheme 1, BP nanoparticles were prepared via a liquid exfoliation approach, which were further modified with mPEG-NH_2 by the electrostatic adsorption between negatively-charged BP and positively charged mPEG-NH_2. Afterwards, BP-mPEG nanoparticles were coated with HA by an amido linkage between amino BP-mPEG with carboxylic HA. We hypothesized that HA (MW = 5000 Da) modified BP nanoparticles (HA-BP) possessed high photothermal conversion efficiency and excellent photothermal stability. HA modification can not only enhance CD44 receptor-mediated endocytosis of BP nanoparticles, but also can repolarize TAMs from the M2 phenotype towards the M1 phenotype to significantly improve tumor immunotherapeutic efficacy. Besides, phototherapy could elicit immunogenic cell death (ICD) to mediate anti-tumor immunity, the dying cells could secrete Damage-associated molecular patterns (DAMPs), including surface-exposed calreticulin (CRT), ATP, and high-mobility group protein B1 (HMGB1), to promote prominent DC maturation, and then induced the activation of specific effector T cells (such as $CD4^+/CD8^+$ T cells) to further eliminate tumor cells [43,44]. In general, this multifunctional nanomaterial can achieve combined PDT/PTT therapy and immunotherapy under the guidance of photoacoustic and fluorescence dual-modality imaging.

2. Experimental section

2.1. Materials

The BP bulk crystals were obtained from Nanjing MKNANO Tech Co. Ltd (purity ≥ 99.995%). *N*-methyl-2-pyrrolidone (NMP ≥ 99.5%), methoxypolyethylene glycol amine (mPEG-NH_2, Mw = 5000), thiazolyl Blue Tetrazolium Bromide (MTT) and diphenylisobenzofuran (DPBF) were obtained from Aladdin Reagents. Sodium hyaluronate (HA, Mw = 5000 Da) was purchased from Bloomage Freda Biopharm. Carbodiimide hydrochloride (EDC·HCL), *N*-Hydroxysuccinimide (NHS), 2′, 7′-dichlorofluorescein diacetate (DCFH-DA), Fluorescein isothiocyanate isomer (FITC), methylene blue (MB) and coumarin-6 (C6) were obtained from Sigma-Aldrich. Fetal bovine serum (FBS), H-DMEM, trypsin–EDTA, 4′, 6-diamidino-2-phenylindole (DAPI) and Calcein AM/PI were purchased from Gibco Life Technologies. Annexin V-FITC Apoptosis Detection Kit was bought from BD Pharmingen. Mice Anti-CD86/PE and mice Anti-CD206/FITC antibody were purchased from BioLegend Co. Ltd. Recombinant Murine IL-4 was obtained from Pepro Tech Co. Ltd (USA) and Lipopolysaccharide (LPS) was bought from Solarbio Life Sciences. Rabbit anti-calreticulin (anti-CRT) antibody was purchased from Cell Signaling Technology (USA). ATP Determination Kit and HMGB1 ELISA Kit were purchased from Life technologies (USA).

2.2. Synthesis of HA-BP nanoparticles

The BP nanoparticles were prepared from bulk black phosphorus through the sonication liquid exfoliation. Briefly, solid BP was dispersed in NMP (1 mg/mL). The mixture was sonicated with an ultrasonic cell disruption apparatus (1200 W, S-4000, with probe) in an ice bath for 10 h, then with an ultrasonic cleaning for 10 h (300 W). Afterwards, the resulted mixture was centrifuged (4000 rpm, 10 min) to remove the oversized bulk BP. The suspension was further centrifuged (13,000 rpm, 30 min) and the precipitate was washed with deionized water and freeze-dried in vacuum.

BP nanoparticles (20 mg) and mPEG-NH_2 (20 mg) were dispersed into deionized water and sonicated for 30 min and then stirring for 4 h. The mixture was then centrifuged at 13,000 rpm for 10 min three times to remove unreacted mPEG-NH_2 and freeze-dried to get mPEGylated BP nanoparticles (BP-mPEG). To get HA-BP, 20 mg BP-mPEG and 20 mg HA were dissolved into 20 mL of formamide and sonicated for 30 min, followed by addition of EDC·HCL (138.4 mg) and NHS (82.4 mg) and stirring. Afterwards, trimethylamine (180 μL) was added dropwise into the above activated mixture under 4 °C, which was continuously stirred for 12 h. Pre-cooled acetone (80 mL) was added into the mixture in an ice bath to crystallize floc formed of HA-BP. The mixture was centrifuged at 13,000 rpm for 10 min three times and freeze-dried to obtain the HA-BP nanoparticles.

To determine the ratio of mPEG-NH_2 coated on the BP nanoparticles, FITC-PEG-NH_2 was used instead of mPEG-NH_2, the preparation method of FITC-PEG/BP was as same as the BP-mPEG. Then the fluorescence peaks at 560 nm was used to determine FITC concentration by a fluorescence spectrometer (FS5, Edinburch), the ratio of FITC-PEG-NH_2 coated on the BP nanoparticles was calculated by the formula: loading efficiency = $W_{FITC-PEG-NH2}/(W_{FITC-PEG-NH2} + W_{BP})$.

Similarly, the amount of HA coated on BP-mPEG was also determined via the same technology. HA-FITC was used instead of HA, the ratio of HA-FITC coated on the BP-mPEG nanoparticles was calculated by the formula: loading efficiency = $W_{HA-FITC}/(W_{HA-FITC} + W_{BP-mPEG})$.

2.3. Characterization

Morphology of BP and HA-BP was observed by transmission electron microscope (TEM) on a H7650 transmission electron microscope (Japan). The UV–vis spectra was performed with a DU-730 spectrophotometer (Beckman, USA). Fourier transform infrared (FTIR) was detected by a Magna-560 spectrometer. The hydrodynamic diameter and zeta potential of the nanoparticles were determined using Nano zetasizer (Malven, UK). The crystal structure was monitored by X-ray diffraction (XRD) using a X'TRA diffractometer (ARL, Switzerland). X-
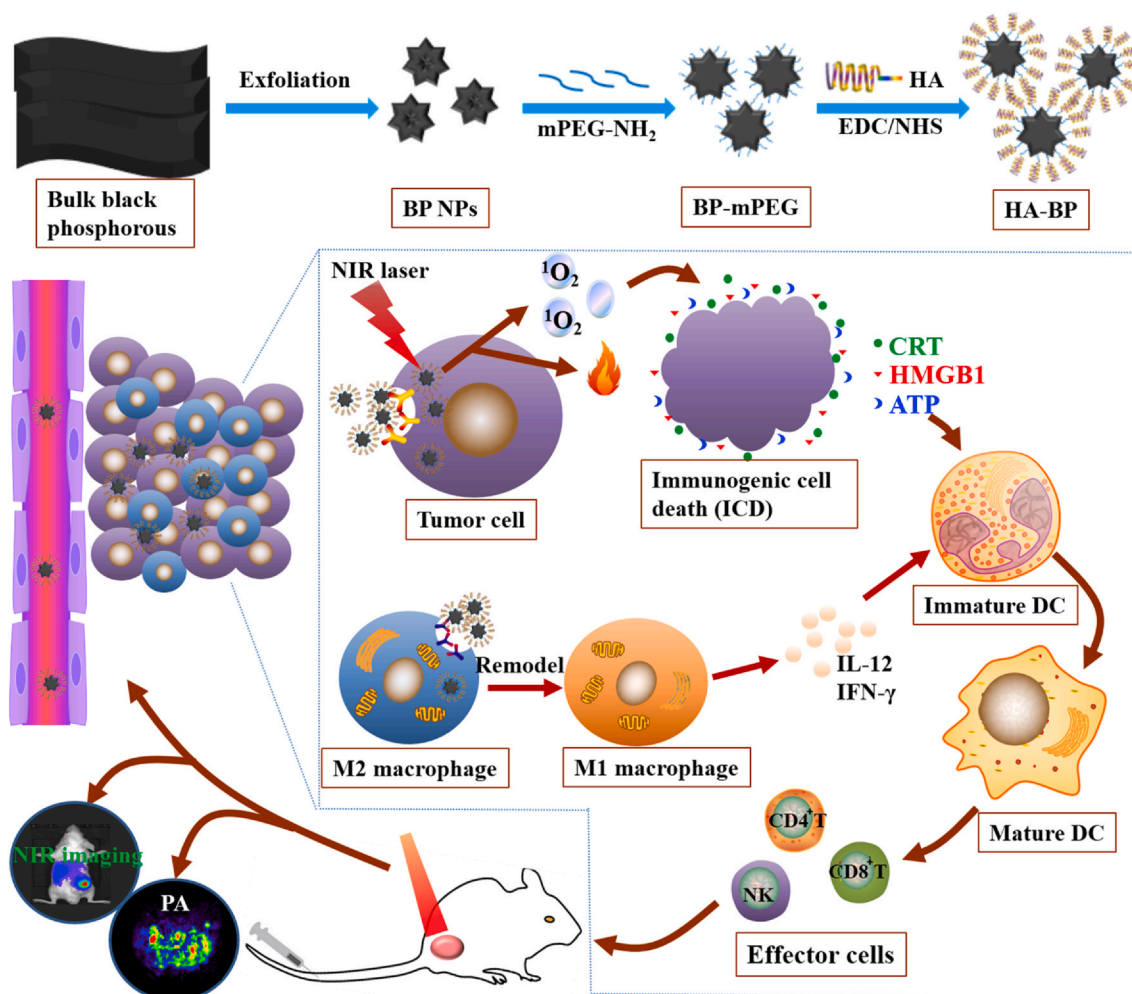
Scheme 1. The synthetic scheme of HA-BP nanoparticles and the function of HA-BP nanoparticles *in vivo*.

ray photoelectron spectroscopy (XPS) was evaluated by a Thermo Scientific instrument (ESCALab 250, USA).

2.4. Evaluation of the photothermal effect and photostability in vitro

The photothermal effects of BP and HA-BP nanoparticles induced by 808 nm laser irradiation were investigated. Sample (2 mL) with various concentrations in transparent quartz plate were irradiated with 808 nm laser (1.5 W/cm²) for 10 min, the temperature was monitored by a thermometer.

The photothermal stability of BP and HA-BP with the same concentration of BP (50 μg/mL) was investigated by irradiating with 808 nm laser (1.5 W/cm²) for 5 min and cooling to initial temperature without irradiation, which repeated five times. To examine the influences of ambient conditions on the stability of BP and HA-BP nanoparticles, the BP and HA-BP nanoparticles were dispersed in water and their photothermal heating cures were recorded after incubation for various periods of time (0, 2, 4, 6 and 8 days) and then exposed to 808 nm laser irradiation for 10 min.

For *in vitro* photostability, the BP and HA-BP nanoparticles with the same concentration of BP (50 μg/mL) were dispersed in water and maintained in a closed tube, then the dispersion was exposed 808 nm laser (1.5 W/cm²) for 10 min, the size change of BP and HA-BP nanoparticles was evaluated for different periods of time (0, 2, 4, 6 and 8 days) by zetasizer, and the morphology of BP and HA-BP nanoparticles after 808 nm laser irradiation for 10 min was immediately measured by

TEM.

For *in vitro* imaging, PA signal of various concentrations (0.05, 0.1, 0.4 and 0.5 mg/mL of HA-BP nanoparticles was detected at 690 nm by a preclinical photoacoustic computerized tomography scanner (Vevo 2100 LAZR, Visual Sonics).

2.5. Evaluation of singlet oxygen

DPBF was employed as a chemical probe to evaluate the generation of ROS. In brief, BP or HA-BP (BP: 50 μg/mL) was mixed with DPBF anhydrous ethanol solution (20 μg/mL). The resulting mixture was kept in darkness and irradiated with lasers at 635 nm (0.5 W/cm²) and 808 nm (1.5 W/cm²), respectively. The UV–vis spectra of DPBF was recorded at about 410 nm at various time points (0, 2, 5, 10, and 20 min).

Singlet oxygen quantum yields (Φ_Δ) were also detected by monitoring the DPBF. Briefly, the oxygen-saturated solution containing BP or HA-BP (BP: 50 μg/mL) or methylene blue (MB) mixing with DPBF (20 μg/mL) were kept in the dark and irradiated with 635 nm laser (0.5 W/cm²) or 808 nm laser (1.5 W/cm²) for 3 min in an interval of 30 s. The ΔOD of DPBF oxidation at 410 nm was detected by UV–vis spectrophotometer. The Φ_Δ values of BP and HA-BP were evaluated by the MB in DMF ($\Phi_\Delta = 0.52$) as the standard [45,46].

2.6. Tumor-associated macrophage polarization

RAW264.7 cells were incubated in DMEM medium (containing 1 μg/mL of LPS) for 48 h to generate M1 macrophages, and were treated with 50 ng/mL of IL-4 for 24 h to obtain M2 macrophages. Then, the resulted macrophages were stained with CD86/PE (dilution 1:200) and CD206/FITC (dilution 1:100) double dye for 30 min. After being washed twice with PBS, cells were fixed with 4% paraformaldehyde for 10 min and then stained with 10 μg/mL DAPI for 10 min. The staining results were observed via confocal laser scanning microscope (CLSM, TCS sp5, Leica). Besides, in order to quantitative determination of the conversion ratio, RAW264.7 cells were treated LPS or IL-4 and stained with CD86/PE (dilution 1:200) and CD206/FITC (dilution 1:100) dye for 30 min, then cells were washed twice with PBS and collected, the M1/M2 ratio was assessed by flow cytometry (FACSCalibur, BD). Furthermore, to investigate whether HA-BP nanoparticles could prime M2 macrophages toward M1 macrophages, M2 macrophages were incubated with HA, BP or HA-BP (HA and BP concentration: 50 μg/mL, HA-BP concentration: 100 μg/mL) for 3 h, laser groups were exposed to 808 nm (1.5 W/cm^2, 3 min) and 635 nm (0.5 W/cm^2, 5 min) laser. Then washed with PBS, the cells were incubated with CD86/PE and CD206/FITC double dye for 30 min. Finally, the ratio of M1/M2 was measured by flow cytometry and CLSM.

2.7. Determination the level of IL-10 and IL-12

To obtain M2 phenotype macrophages, RAW264.7 cells were incubated with IL-4 (concentration: 50 ng/mL) for 24 h, and then the obtained M2 macrophages were treated with HA, BP or HA-BP (BP concentration: 50 μg/mL) for 4 h to polarize to M1 macrophages, laser groups were exposed to 808 nm (1.5 W/cm^2, 3 min) and 635 nm (0.5 W/cm^2, 5 min) laser. Afterwards, the cells were incubated with serum-free DMEM medium for 24 h, the supernatant medium was collected and measured by mouse IL-10 and IL-12 Elisa kits.

2.8. In vitro cellular uptake

The cellular internalization by 4T1 cells was evaluated by flow cytometry and CLSM. Briefly, 4T1 cells were incubated with BP/C6 or HA-BP/C6 (concentration of BP: 50 μg/mL) at 37 °C for various time intervals. Besides, to verify the targeting specificity, 4T1 cells were pre-cultured with HA (concentration: 100 μg/mL) for 3 h and then incubated with HA-BP/C6 at the same dose for different time. Then, the cells were washed twice and fixed with 4% paraformaldehyde for 10 min. Afterwards, the cells were stained with 10 μg/mL of DAPI solution for 10 min and imaged by CLSM. The final quantitative analysis was conducted by flow cytometry.

2.9. In vitro cellular ROS and thermal imaging study

DCFH-DA was applied to assess the level of intracellular ROS. Firstly, 4T1 cells were treated with BP or HA-BP with same concentration of BP (50 μg/mL) for 4 h, then cultured with DCFH-DA for 30 min. Afterwards, the cells of laser groups were exposed to 635 nm laser (0.5 W/cm^2) for 5 min or 808 nm laser (1.5 W/cm^2) for 2 min. The cells were washed twice with PBS and stained with DAPI (10 μg/mL) for 10 min. The fluorescence images were examined by CLSM, and the flow cytometry was also utilized to quantify the production of ROS.

To evaluate the photothermal effect of HA-BP in 4T1 cells, the cells were incubated in a 6-well plate and treated with BP and HA-BP (BP concentration: 50 μg/mL) for 4 h, followed by replacing with fresh culture DMEM medium. Then the plates were irradiated with 808 nm laser (1.5 W/cm^2) for 3 min, the infrared thermal imaging camera (Ti27, Fluke) was utilized to record the change of temperature.

2.10. In vitro live/dead state detection

Live/dead state detection was carried out in 12-well plates by Calcein-AM/PI staining Kits. 4T1 cells were treated with BP and HA-BP (BP concentration: 50 μg/mL) for 4 h, the laser groups were irradiated with 635 nm (0.5 W/cm^2, 5 min) and 808 nm laser (1.5 W/cm^2, 2 min). After incubation for 24 h, the cells were cultured with Calcein-AM (0.67 μmol/L) and PI (1.5 μmol/L) in Buffer solutions for 15 min. The fluorescence images were recorded with a fluorescence microscope.

2.11. Wound healing assay

Before wound healing assay, condition medium was prepared in advance. Firstly, RAW264.7 cells were incubated with IL-4 for 24 h to obtain M2 macrophages, then old medium was replaced with fresh DMEM medium containing 50 μg/mL of BP or HA-BP. After incubation for 4 h, the medium was collected as the corresponding condition medium. Simultaneously, M2 medium without treatment was defined as M2 condition medium.

Wound healing assay was conducted to measure the effect on 4T1 cells migration capacity after different treatments. In brief, 4T1 cells (1 × 10^5 cells/per well) were plated in a 6-well plate for 24 h, the cell monolayers were wounded and incubated with fresh serum-free medium. After that, the cells were incubated with M2, BP condition medium or HA-BP condition medium. The healing status were observed at 0 and 24 h. Migration rate of 4T1 cells was computed by the formula: Migration = [(Scratch area at 0 h - Scratch area at 24 h)/Scratch area at 0 h] × 100%.

2.12. Motility and invasion assay

Motility and invasion assay were implemented via transwell experiment to detect the metastasis and invasion capacity of 4T1 cells. For the cell motility assay, 4T1 cells (5 × 10^3 cells/per well) were seeded in the upper transwell chambers and were incubated with fresh serum-free DMEM medium, M2 condition DMEM medium, BP condition DMEM medium or HA-BP condition DMEM medium. Then fresh DMEM medium containing 600 μL of 10% FBS was added into the lower chamber. After incubated for 24 h, removed un-migrated cells on the upper surface of the membrane, and the cells of the lower side of the membrane were fixed, stained with crystal violet and observed by a microscope (NIKON TS-100). Finally, 35% acetic acid was utilized to dissolve the stained cells and the final absorbance was detected at 570 nm. The cell invasion assay was performed in the same way but with a matrigel-coated transwell chamber. Invasion and migration rates were computed as the ratio of OD value of experiment group to that of control group.

2.13. Cytotoxicity evaluation

Preparation of different condition medium: RAW264.7 cells were incubated with IL-4 for 24 h, then old medium was replaced with fresh medium containing 50 μg/mL of BP or HA-BP, the medium was collected as condition medium after cells was incubated for 4 h. Meanwhile, M2 medium without treatment was defined as M2 condition medium, and M1 medium without treatment was defined as M1 condition medium.

The cytotoxicity of BP and HA-BP nanoparticles was detected by MTT assay. Briefly, 4T1 cells were treated with BP or HA-BP at different concentrations of BP (5, 20, 50 or 100 μg/mL) and exposed to 635 nm (0.5 W/cm^2, 5 min) laser and 808 nm (1.5 W/cm^2, 2 min) laser, respectively. Followed by incubated for 24 h, the fresh DMEM medium containing MTT (5 mg/mL) was added and continued to be cultured for another 4 h. Then removed the medium and added 150 μL of DMSO per well, the OD value at 570 nm was recorded with microplate system. In addition, the cytotoxicity of M1, M2, BP condition medium (BP + M2)

or HA-BP condition medium (HA-BP + M2) on 4T1 cells was also evaluated by MTT method.

2.14. Cell apoptosis assay

4T1 cells were incubated with BP, HA-BP, BP condition medium (BP + M2) or HA-BP condition medium (HA-BP + M2) for 4 h, the laser was performed according to MTT assay. After incubation for 24 h, 4T1 cells were collected and re-suspended in PBS containing Annexin V-FITC (15 μL) and PI (5 μL) for 15 min in dark environment. The fluorescence intensity signal was detected by a flow cytometer.

2.15. In vitro detection of ICD biomarkers

The membrane surface-exposure of CRT was firstly analyzed by flow cytometry. Briefly, 4T1 cells were treated with BP, HA-BP, BP condition medium (BP + M2) or HA-BP condition medium (HA-BP + M2) for 4 h and then exposed to laser as in section 2.14. Followed by incubated for 24 h, the cells were incubated with anti-CRT antibody for 30 min and collected. The samples were detected using flow cytometry. The HMGB1 Elisa Kit and ATP Determination Kit were utilized to determine the extracellular release of HMGB1 and ATP, respectively. Typically, 4T1 cells were treated with BP or HA-BP nanoparticles for 4 h, and the laser was performed according to MTT assay. After incubation for 24 h, the supernatant medium was analyzed via HMGB1 Elisa Kit and ATP Determination Kit, respectively.

2.16. In vitro DC maturation

DC maturation experiments were investigated by transwell method. Briefly, 4T1 cells were plated in upper chamber of a 24-well plate at a cell density of 5×10^4 cells per well, and DCs were seeded at 1×10^5 cells per well in lower chamber. After co-cultured for 12 h, BP and HA-BP were added into upper chambers at the same concentrations of BP (50 μg/mL). 4T1 cells were treated with the laser after 4 h co-incubation as in section 2.14. After incubation for 48 h, DCs were incubated with anti-CD86/PE and MHCII/FITC antibodies for 30 min and collected, the fluorescence intensity was detected by a flow cytometer.

2.17. In vivo fluorescence and PA imaging

All Female mice (BALB/c) were approved and bought from Sun Yat-sen University animal center. A suspension of 100 μL 4T1 cells (1×10^6) was made and injected into right lower abdomen of the mouse to construct 4T1 cancer-bearing xenograft mouse model. When tumor volumes of 4T1 cancer-bearing mice reached 100 mm^3, the mice were administrated with DIR (1,1-dioctadecyl-3,3,3,3-tetra-methylindotricarbocyaine iodide, 0.25 mg/kg), BP/DIR (2 mg/mL) or HA-BP/DIR (2 mg/mL). The fluorescence images were recorded by IVIS Lumina Vivo Imaging System with the excitation wavelength at 740 nm and the emission filter at 790 nm at various time points (1 h, 2 h, 4 h, 8 h, 12 h, 24 h and 48 h). Finally, all tumors and major tissues were excised and imaged after 48 h administration.

To further evaluate the HA-BP nanoparticles accumulation inside tumor, HA-BP nanoparticles were imaged at 690 nm before and after intravenous injection with BP or HA-BP nanoparticles (BP concentration: 2 mg/kg) to 4T1 cancer-bearing mice by a preclinical photoacoustic computerized tomography scanner (Vevo 2100 LAZR, Visual Sonics).

2.18. In vivo anticancer evaluation

Female mice (BALB/c) implanted with subcutaneous 4T1 breast-tumor xenografts were utilized as the animal model. When the tumor volume reached 100 mm^3, the mice (n = 6) were randomly divided into ten groups as follows: ① Control, ② Control + 808 + 635 nm laser, ③

BP, ④ BP + 808 nm laser, ⑤ BP + 635 nm laser, ⑥ BP + 808 + 635 nm laser, ⑦ HA-BP, ⑧ HA-BP + 808 nm laser, ⑨ HA-BP + 635 nm laser, ⑩ HA-BP + 808 + 635 nm laser. BP or HA-BP (2 mg/mL, 100 μL) were administrated into mice through intravenous injection every 2 days for 5 times. Then the tumor sites of mice in the laser groups were exposed to 808 nm laser (1.5 W/cm^2, 3 min) and 635 nm laser (0.5 W/cm^2, 5 min) after injection for 4 h. The temperature changes in tumor sites were recorded by an infrared thermal camera. The tumor sizes and body weight were measured every two days and tumor volumes were measured by the equation: V = (length) × (width)^2/2. The Kaplan-Meier survival curves were obtained by the percent mice when the tumor volume **>** 1200 mm^3 or the mice died. After 21 days, tumor tissues of all groups were dissected and soaked in 4% formalin, embedded with paraffin for immunofluorescence staining of Ki67, CD31 and MMP-9. To assess the effect of HA-BP nanoparticles on the polarization of TAMs, tumors were stained by CD86/PE and CD206/FITC antibodies to identify the distribution of M1 and M2 macrophages in the tumor sites. Besides, tumors were also stained with anti-CD4/PE and anti-CD8/FITC antibodies to evaluate the effect of immunotherapy. The other major organ tissues (containing heart, liver, spleen, lung, kidney and brain) were also stained with hematoxylin and eosin (H&E).

2.19. Statistical analysis

All experimental data was expressed in this manuscript as mean ± standard deviation. The difference between two groups was analyzed by a two-tailed Student's *t*-test. The statistical analysis was performed by Origin 8.5.

3. Results and discussion

3.1. Characterization of HA-BP nanoparticles

The synthesis process of HA-BP nanoparticles was shown in Fig. 1A, BP nanoparticles were firstly modified with mPEG-NH$_2$, then HA-BP nanoparticles were obtained by covalently linking between the amino of BP-mPEG and the carboxyl of HA. As revealed in Fig. 1B, BP nanoparticles with diameter of 30 nm were obtained (Fig. 1D). To improve the dispersibility, BP nanoparticles were modified with mPEG-NH$_2$ via electrostatic interaction, the size of BP nanoparticles increased to about 50 nm with a uniform distribution (Fig. S1A). And the typical *N*–H bending vibration peak at 1640 cm^{-1}, P–P–O stretching band at 1100 cm^{-1} as well as P=O stretching vibration band at 1040 cm^{-1} in FITR spectrum further confirmed the successful synthesis of BP-mPEG nanoparticles (Fig. S1B). In order to enhance the targeting ability and biocompatibility of BP-mPEG nanoparticles, low molecular weight HA (MW = 5000 Da) was used to coat on the surface of BP-mPEG nanoparticles via amide bond. As shown in Fig. 1C and E, HA-BP nanoparticles showed a larger particle size of 56 nm. The zeta potential of BP increased from − 23.7 mV to − 6.03 mV after modification with mPEG-NH$_2$, and then decreased to − 28.4 mV after functionalization with HA (Fig. 1F), proving the successful fabrication of HA-BP nanoparticles. Besides, the crystal structures of BP and HA-BP nanoparticles were measured by XRD, all the characteristic periodic peaks in the pattern were consistent with those of orthorhombic BP (standard JCPDS card no. 6524-91, Fig. 1G). The chemical constitutions of HA-BP nanoparticles were determined by XPS (Fig. S2A-E). Fig. S2A showed the binding energies of various elements after calibration with the binding energy of C1s peak at 284.8 eV. The main component elements mainly included C, O, N and P. The two peaks at 130.3 eV and 129 eV were attributed to the P2p$_{1/2}$ and P2p$_{3/2}$ doublets of zero-valence P in the P2p spectrum, respectively. The N1s spectrum showed the binding energy of *N*–H at 399.6 eV, and the binding energy of C=O at 532.02 eV was shown in O1s spectrum, further demonstrating the successful HA capping of BP nanoparticles. Furthermore, the conjugation was further characterized by FTIR spectrum (Fig. 1H). BP
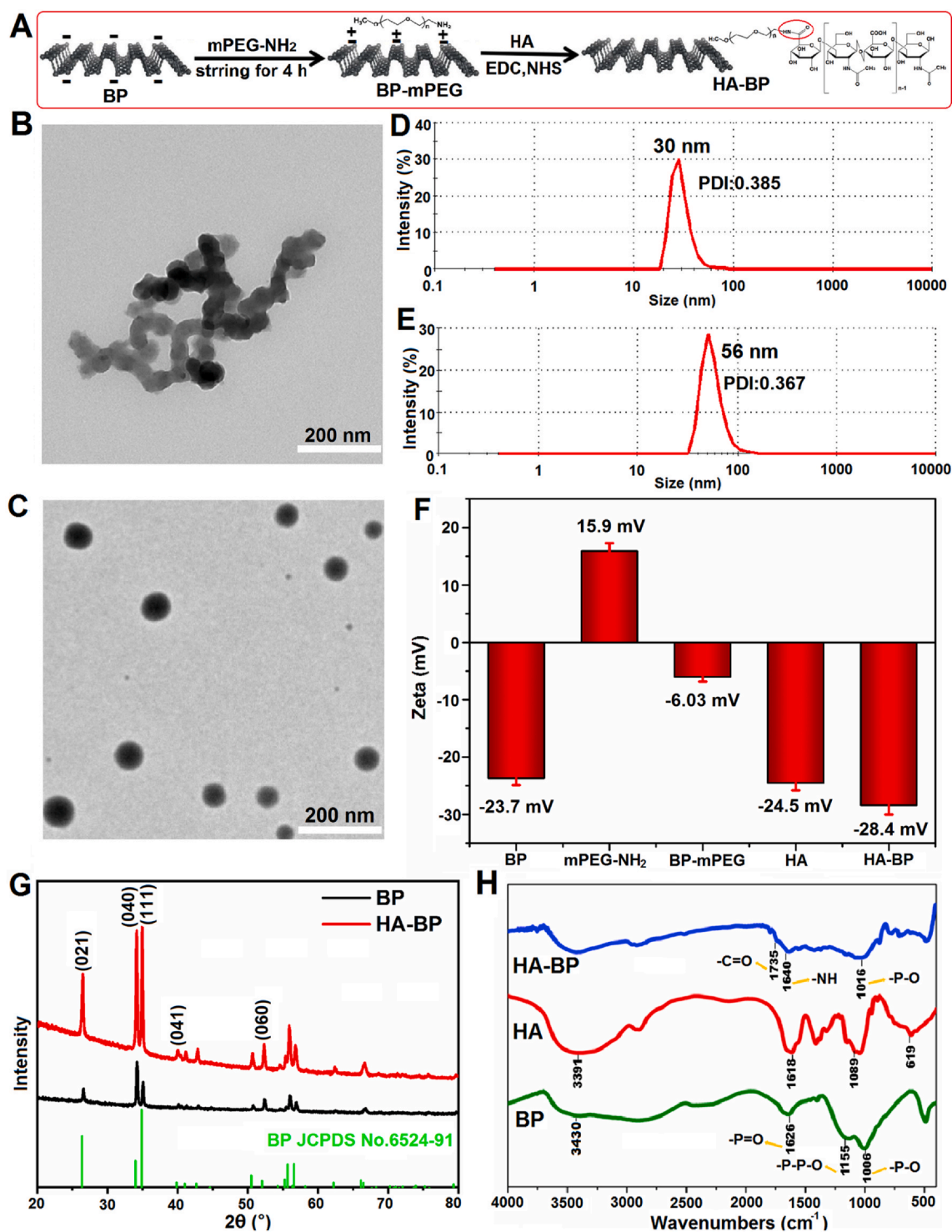
Fig. 1. (**A**) The synthesis schematic of HA-BP nanoparticles. (**B**) TEM image of BP nanoparticles. (**C**) TEM image of HA-BP nanoparticles. (**D**) Particle size of BP nanoparticles. (**E**) Particle size distribution of HA-BP nanoparticles. (**F**) Apparent zeta potential of BP, mPEG-NH$_2$, BP-mPEG, HA and HA-BP. (**G**) XRD image of BP and HA-BP nanoparticles. (**H**) FTIR spectrum of BP, HA and HA-BP.

comprised the broad absorption bands at 1006 cm^{-1} and 1155 cm^{-1} appointing to P–O stretching band and P–P–O linear stretching band, respectively, and the small peak of 1626 cm^{-1} was stemmed from the P=O stretching vibration band. Anti-symmetric and symmetric stretching vibration peaks of C=O at 1615 cm^{-1} and 1409 cm^{-1} were observed from the FTIR spectrum of HA. The FTIR results of HA-BP retained all characteristic peaks of BP, which confirmed the successful synthesis of HA-BP through the amide bond containing C=O stretching

vibration peak of 1735 cm^{-1} as well as *N*–H bending band of 1640 cm^{-1}, and the intensity of C=O symmetric stretching vibration at 1409 cm^{-1} from the FTIR spectrum of HA was obviously weakened, which could be ascribed to the formation of the amide bond. The amount of mPEG-NH$_2$ coated on HA-BP nanoparticles was calculated to be 21.1% (w/w %) of the HA-BP, and the ratio of HA and BP in HA-BP nanoparticles was 39.2% (w/w %) and 39.7% (w/w %), respectively. Furthermore, Fig. S3 showed the size and PDI of BP and HA-BP
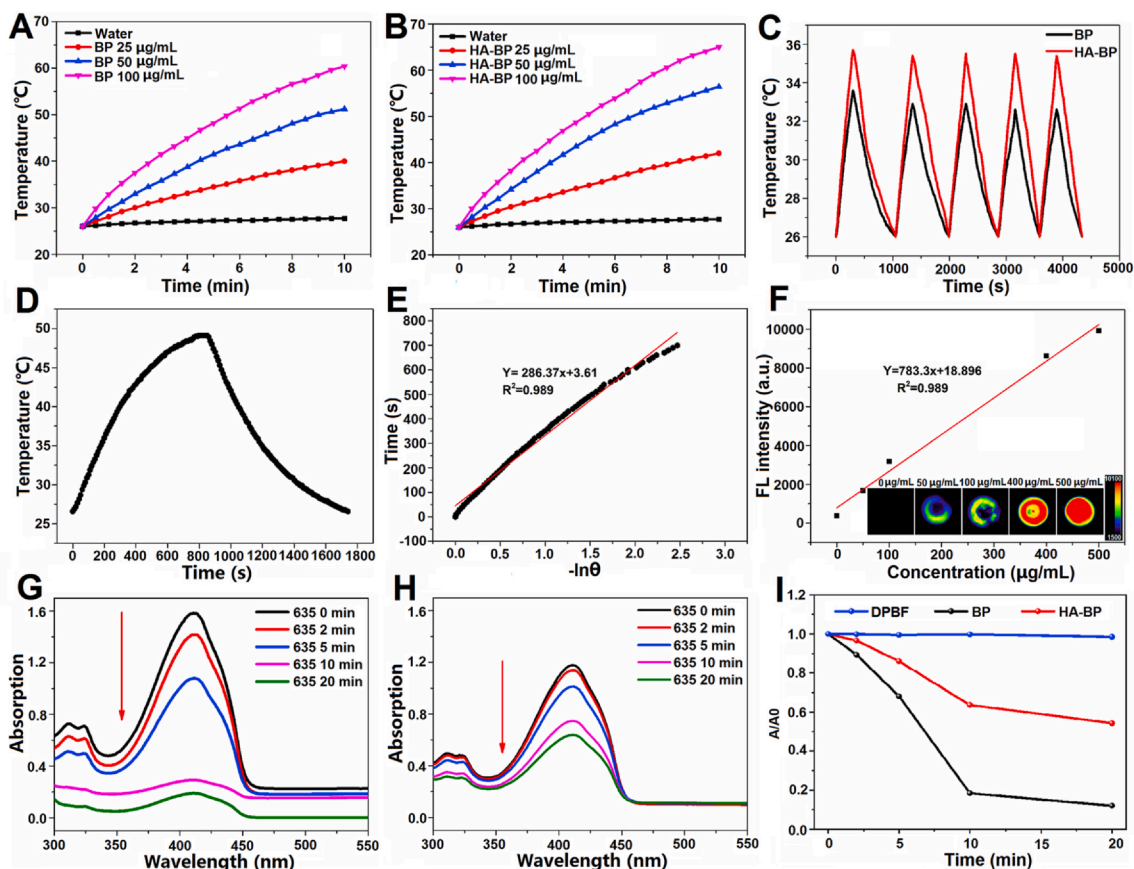
Fig. 2. Photothermal heating curves of ultrapure water, BP (**A**) and HA-BP (**B**) aqueous dispersions with various concentrations at 808 nm laser (1.5 W/cm^2). (**C**) Five cycles of temperature variation of BP and HA-BP solution (25 μg/mL) with continuous 808 nm laser irradiation (1.5 W/cm^2, 5 min) and natural cooling. (**D and E**) The photothermal conversion efficiency of HA-BP nanoparticles. (**F**) Linear fit of PA intensity to the HA-BP concentration at 690 nm. Inset is the corresponding PA images. Time-course UV–vis absorption spectrum of DPBF solution with BP (**G**) and HA-BP (**H**) under 635 nm laser (0.5 W/cm^2) irradiation. (**I**) Photo-irradiation time dependent A/A0 of the $^1O_2$ indicator DPBF incubated with BP and HA-BP nanoparticles.

nanoparticles in PBS, which indicated that HA capping could ameliorate the stability of BP nanoparticles and keep BP highly stable in physiological solutions for at least 8 days.

3.2. Photothermal effect and photostability of HA-BP nanoparticles

To assess the photothermal effects of BP and HA-BP nanoparticles, the aqueous dispersions of nanoparticle at different BP concentrations were irradiated with 808 nm laser at a power intensity of 1.5 W/cm^2 for 10 min. Fig. 2A showed a concentration-dependent and time-dependent photothermal effects of BP solution. The temperature of BP nanoparticles dispersion rapidly increased by 14 °C after exposed to laser for 10 min even at a low concentration of 25 μg/mL, while the temperature of water increased slightly ($\Delta T \approx 1.7$ °C). In comparison with the bare BP nanoparticles, HA-BP heated up faster (Fig. 2B) at the same condition, exhibiting a better photothermal capability. This was probably due to the HA shell that reduced the degradation and aggregation of BP nanoparticles. The photothermal stability of HA-BP was measured as seen from Fig. 2C, the HA-BP nanoparticles presented a better photothermal stability than that of BP nanoparticles, there was no obvious change of photothermal effects with HA-BP nanoparticles during five heating cycles. The time-dependent photothermal stabilities of BP and HA-BP nanoparticles were further examined (Fig. S4A and B). We observed that the temperature of BP solution increased by 25.2 °C under 808 nm laser (1.5 W/cm^2) irradiation for 10 min on the first day, but the temperature only increased by 7.7 °C after storing for 8 days, which was likely due to the degradation of BP nanoparticles. In comparison, the temperature of HA-BP solution still increased by 26.5 °C after

irradiation for 10 min on the 8th day, a result close to that of the first day (30.4 °C). This suggested that HA shell could improve BP stability in aqueous dispersion even with NIR light irradiation. For further quantitative comparison, the photothermal conversion efficiency of HA-BP nanoparticles was calculated as 46.05% (Fig. 2D and E), which was higher than that of the bulk BP nanoparticles (29.47%, Fig. S4C and D). Additionally, the corresponding photostability of BP and HA-BP nanoparticles was further evaluated and shown in Fig. S5, the size of BP nanoparticles reduced constantly after 808 nm laser irradiation, and the morphology of the BP nanoparticles was partly destructed right after 808 nm laser irradiation (Fig. S5A and B). While almost no evident size or morphological change was observed in HA-BP nanoparticles group (Fig. S5A and C), suggesting that HA capping could improve the photostability of BP nanoparticles. Overall, the results indicated that HA modification could effectively improve the stability and photothermal efficiency of BP nanoparticles.

To investigate the bioimaging performance of HA-BP, *in vitro* PA imaging experiment was conducted and displayed in Fig. 2F. The PA signal intensities of HA-BP aqueous dispersions were related positively to HA-BP concentrations at 690 nm laser excitation. Therefore, HA-BP nanoparticles could be used as a PA contrast agent for bioimaging.

3.3. Photodynamic effect of BP and HA-BP

The $^1O_2$ generation capacity is vital for the PDT efficiency, so DPBF was used as the singlet oxygen probe to detect the photodynamic performances of BP and HA-BP. With the increase of $^1O_2$, the absorbance of DPBF in 410 nm would decrease. As presented in Fig. 2G and H, the

decrease of DPBF absorbance intensity with a prolonged time verified the generation of $^1O_2$ by BP or HA-BP nanoparticles under NIR laser irradiation. According to the quantification result (Fig. 2I), the decrease of DPBF in pure DPBF group was negligible, indicating no ROS generation. While the relative absorbance of BP group decreased to 12.0% in 20 min under the same conditions, HA-BP generated less ROS than BP, this was probably because of HA capping that enhanced the photothermal conversion efficiency of BP nanoparticles and hindered the energy transfer between BP and oxygen for generating $^1O_2$ [47]. Meanwhile, $^1O_2$ generation efficiency of BP and HA-BP nanoparticles under 808 nm laser irradiation (1.5 W cm^2) was also evaluated (Fig. S6), and the result indicated that $^1O_2$ generation efficiency of BP and HA-BP nanoparticles under 635 nm laser irradiation is significantly better than that with 808 nm laser irradiation. The $^1O_2$ quantum yield (Φ_Δ) of BP and HA-BP under 635 nm laser irradiation was calculated to be 85.2% and 41.6%, respectively, using MB as the standard [45], while the Φ_Δ of BP and HA-BP under 808 nm laser irradiation was only 7.5% and 4.3%, respectively (Fig. S6C). The difference could be attributed to the energy transfer of photo-excited electrons caused by 808 nm laser, which is mainly released in the form of the heat, while the energy transfer caused by 635 nm laser mainly reacts with oxygen molecules to produce $^1O_2$ [20,48].

3.4. Tumor-associated macrophage polarization

It was known that HA with low molecular weight could activate macrophages and remodel M2 macrophages toward M1 macrophages [40]. Therefore, we investigated whether HA-BP nanoparticles had an immunological effect on macrophages polarization. Firstly, to verify whether if HA-BP nanoparticles could be internalized by M2 macrophages or not, RAW264.7 cells were pretreated to generate M2 macrophages, C6 was used as a fluorescence probe to identify the internalization of BP and HA-BP nanoparticles by flow cytometry analysis (Fig. S7). We observed that the intracellular fluorescence intensity all presented a time-dependent increase. No obvious difference of cellular uptake was observed in the BP/C6 and HA-BP/C6 groups, indicating that both BP and HA-BP nanoparticles were easily endocytosed by M2 macrophages, which benefited the polarization of TAMs from M2 to M1 phenotype. Afterwards, we explored the influences of HA-BP nanoparticles on macrophages polarization. Firstly, we induced RAW264.7 cells into M2 macrophages with 50 ng/mL of IL-4 for 24 h, and incubated them with HA (50 μg/mL), BP (50 μg/mL) and HA-BP (100 μg/mL) for 3 h, then CD206/FITC antibody was used to mark M2 macrophages, CD86/PE antibody was chosen as a typical marker for M1 Macrophages. Flow cytometry analysis was revealed in Fig. 3A and C, RAW264.7 cells expressed 51.7% CD206 and 48.9% CD86, when RAW264.7 cells were treated with IL-4 alone, the expressions of CD206 were increased to 68.3%, while the expressions of CD86 were decreased to 26.9%, implying that ~68.3% macrophages were polarized to M2 phenotype successfully. Next, M2 macrophages were treated with HA, BP, HA-BP, BP + laser or HA-BP + laser, respectively, we observed that the expressions of CD86 were dramatically up-regulated to 71.2%, 86.5% and 87.6% on macrophages treated with HA, HA-BP and HA-BP + laser, respectively, while the expressions of CD206 were decreased to 45.5%, 26.0% and 24.6%, respectively, and BP or BP + laser displayed only a little effect on macrophage polarization. These data indicated that HA-BP could reeducate the polarization of TAMs from M2 to M1 macrophages, which was mainly benefited from the functions of low molecular weight HA, and laser irradiation had no obvious effect on macrophage polarization. Similarly, the polarization was further proved by CLSM (Fig. 3B). When M2 macrophages were treated with HA, HA-BP or HA-BP + laser, the red fluorescence signal (CD86) was obviously enhanced and the green fluorescence signal (CD206) was attenuated. Besides, to further confirm the regulation effect of HA-BP nanoparticles on TAMs subtype, the relevant cytokines of M1 and M2 macrophages were determined using Elisa Kit. After treated with HA,

HA-BP or HA-BP + laser, the level of IL-12, the representative M1-type cytokine, increased apparently (Fig. 3D), and the secretion level of IL-10, a representative M2-type cytokine, decreased obviously (Fig. 3E), while macrophages of HA-BP or HA-BP + laser group secreted slightly higher level of IL-12 and slightly lower level of IL-10 than IL-4-treated group. All above results indicated that HA-BP nanoparticles could effectively polarize M2 macrophages to M1 phenotype.

3.5. In vitro cellular uptake

To manifest the targeting capacity of HA-BP nanoparticles on 4T1 cells (CD44$^+$ over-expressed), the dye C6 was used as a fluorescence probe to mark HA-BP nanoparticles. The cell uptake result of flow cytometry (Fig. S8) and quantitative analysis were shown in Fig. 4A. There was only a slight amount of C6 in cells even at 8 h in free C6 group. In contrast, the internalization level in the BP/C6 group increased with increasing of incubation time, which were still at least 2.5-fold higher than free C6 group all the time. In addition, the mean fluorescence intensity of HA-BP/C6 reached maximum at 4 h, which was 1.84-fold stronger than that of the BP/C6 group, and then slightly decreased at 6 h. The distinct difference indicated the specific and rapid uptake of HA-BP by 4T1 cells, which was because that HA can bind with the CD44$^+$, a highly expressed HA receptor on the surface of 4T1 cell membrane, to improve the active targeting capacity of BP to 4T1 cells. Furthermore, after 4T1 cells were pre-cultured with HA for 3 h, there was no significant difference of the mean fluorescence intensity between BP/C6 and HA + HA-BP/C6 groups at each time point, further indicating HA modified BP possessed higher 4T1 tumor selectivity on account of HA receptor (CD44$^+$)-mediated endocytosis process. Besides, the above flow cytometric results were consistent with CLSM results, the amount of BP/C6 or HA-BP/C6 nanoparticles internalization by 4T1 cells was visualized by green fluorescence. As shown in Fig. 4B, compared with the negligible green fluorescence of C6 alone group, BP/C6 groups exhibited apparent green fluorescence intensity, while 4T1 cells treated with HA-BP/C6 showed the strongest green fluorescence, further indicating that HA capping could improve the tumor targeting ability of BP nanoparticles.

3.6. In vitro photothermal and photodynamic effect

After confirming the targeting efficacy of HA-BP nanoparticles, the photodynamic effects in 4T1 cells was investigated. The intracellular ROS generation was detected using the DCFH-DA kit. DCFH-DA itself is not fluorescent but can be hydrolyzed to DCFH via intracellular esterase. And DCFH molecules could be oxidized to DCF by ROS to emit strong green fluorescence, acting as an indicator of ROS generation. Quantitative flow cytometric analysis was shown in Figure S9. Almost no green fluorescence was observed in Control, Control + 635 nm laser, BP and HA-BP groups at each time interval. While when cells were treated with 635 nm laser at a power intensity of 1.5 W/cm^2 irradiation for 5 min, the mean fluorescence intensities in BP group were lower than that of HA-BP group for all time intervals, indicating that HA-BP nanoparticles generated more ROS than BP nanoparticles. Besides, the cells treated with BP or HA-BP combined with 808 nm plus 635 nm dual laser irradiation exhibited a little stronger fluorescence intensity compared with that after single 635 nm laser irradiation, this was because that PTT improved the effect of PDT for generating more singlet oxygen [49]. Interestingly, the mean fluorescence intensities in HA-BP group plus laser irradiation exhibited strongest fluorescence signal at 4 h and then decreased at 6 h, which was due to the large amount of HA-BP nanoparticles internalization by 4T1 cells at 4 h (Fig. 4A). Besides, the CLSM results of 4T1 cells with green DCF fluorescence were shown in Fig. 4C, there was slight green fluorescence was observed in control groups with or without laser irradiation, while the strong green fluorescence was observed in BP and HA-BP group after 635 nm laser irradiation. Importantly, the fluorescence signal of HA-BP + 635 nm laser
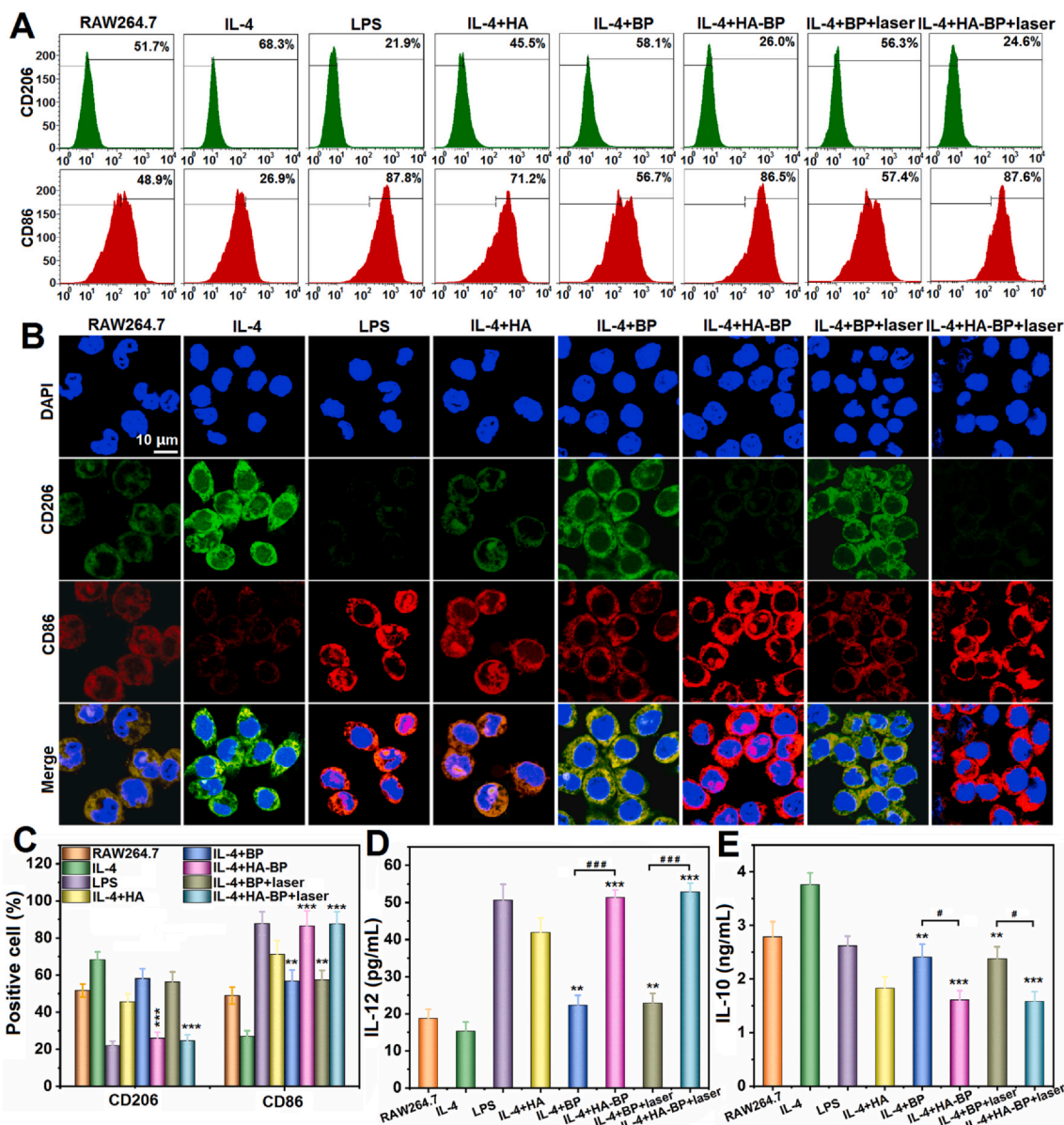
Fig. 3. HA-BP nanoparticles induce M2 macrophages to M1 phenotype: (**A and C**) Flow cytometric results of expression of CD86 (M1) and CD206 (M2) treatment with different formulations. (**B**) Confocal images of expression of CD86 (M1) and CD206 (M2) treatment with different formulations. (**D**) The level of IL-12 released by macrophages before and after regulation of M2 macrophages towards M1 phenotype with different formulations. (**E**) The level of IL-10 secreted by macrophages with different formulations. $*p < 0.05$, $**p < 0.01$ and $***p < 0.001$ as contrast with IL-4 group, and $^{\#}p < 0.05$ and $^{\#\#\#}p < 0.001$.

performed stronger than those of BP + 635 nm laser group, which was attributed to more HA-BP nanoparticles internalization by 4T1 cells than BP nanoparticles owing to HA receptor (CD44$^+$)-mediated tumor targeting capacity. These results lead to the conclusion that HA-BP could enhance the ROS generation capability of cells compared with BP nanoparticles, thereby achieving excellent overall therapeutic effect.

Additionally, Fig. 4D showed that HA-BP could induce intracellular hyperthermia when exposed to 808 nm laser. As expected, the temperature of the blank group only slightly rose to 37.1 °C with 808 nm laser (1.5 W/cm^2, 3 min) irradiation, while the temperature of the experimental groups increased rapidly in the existence of BP and HA-BP nanoparticles. Especially, the temperature of the HA-BP group with the BP concentration of 50 μg/mL could reach as high as 52.2 °C higher than that of BP group (45.5 °C) within 2 min NIR irradiation, which could induce rapid cellular destruction due to protein coagulation, so the laser irradiation of 2 min was performed to evaluate the cytotoxicity of nanoparticles. In general, this result suggested that HA-BP could act

as an outstanding PTT agent against cancer.

For purpose of evaluating visually therapeutic efficiency of HA-BP nanoparticles *in vitro*, Calcein-AM/PI co-stained images (Fig. 4E) were further applied to identify the live/dead states of 4T1 cells. Typically, there were almost no dead cells (red) in the control groups, which confirmed that NIR laser irradiation alone was not harmful to cells. There were small amount of dead cells observed in BP and HA-BP groups, which might be because that BP degrade and produce phosphate anions in the cells, and unabiding elevation of cytosolic phosphate anions influence cellular ATP hydrolysis to cause programmed cell death and inhibit proliferation of tumor cells [50–53]. Besides, in the groups of BP and HA-BP with a single 635 nm or 808 nm laser, a small amount of cells showed orange or red color, suggesting that BP and HA-BP nanoparticles could cause 4T1 cells apoptosis with NIR irradiation. Compared with HA-BP + 808 nm and HA-BP + 635 nm laser groups, there were a larger amount of cells stained red in HA-BP + 808 + 635 nm laser group, most of the cells showed chromatin
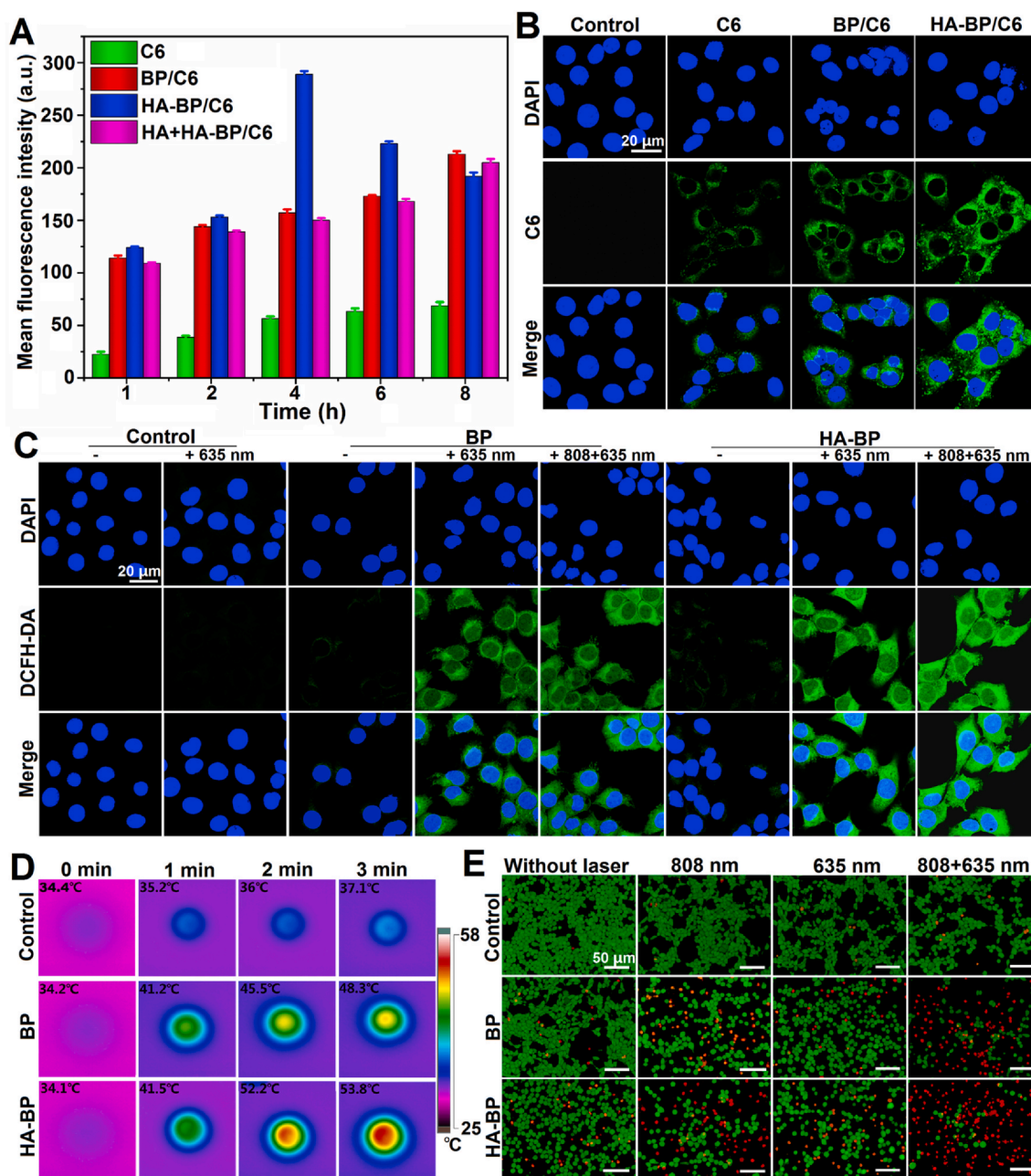
Fig. 4. (**A**) Flow cytometric results of the nanoparticles uptake by 4T1 cells at different time. (**B**) The CLSM images of C6-labeled nanoparticles internalized by 4T1 cells at 4 h. (**C**) CLSM images of intracellular ROS in 4T1 cells with different formulations for 4 h under 635 nm laser (0.5 W/cm^2, 5 min) or 808 nm laser (1.5 W/cm^2, 2 min) irradiation. (**D**) The temperature variation of cells in 6-well plates treated with different formulations for 4 h, before and after 808 nm (1.5 W/cm^2) laser irradiation for different time. (**E**) Calcein-AM/PI staining results with different formulations and irradiation conditions at 24 h.

condensation and irregular shape, which could be explained that PTT increases the separation rate of the electron (hole) and enhances the therapeutic efficiency of PDT, implying an effective phototherapy on 4T1 cells by HA-BP after NIR irradiation.

3.7. Cell migration and invasion assay

The anti-metastatic effects of HA-BP nanoparticles *in vitro* were verified by wound-healing and transwell experiments. As illustrated in Fig. 5A and C, 4T1 cells regrew quickly and the wound recovered rapidly in the blank cells group and M2 condition medium group. Compared with BP + M2 group, HA-BP + M2 treatment dramatically restrained the wound healing rate of 4T1 cells with a wound closure of only 1.7%. This may be due to M1 macrophages re-educated by HA-BP

nanoparticles inhibiting the migration of 4T1 cells. In addition, the transwell experiment was implemented to further determine the influence of HA-BP nanoparticles on invasion and migration capacity of 4T1 cells (Fig. 5B and D). We found that cells passed through the membrane and covered almost the entire lower surface in the blank group and M2 condition medium group. The invasion and migration rates of M2 group were 1.51 and 1.067, respectively, indicating the strong invasion and migration capacity of 4T1 cells. However, after treatment with HA-BP + M2, the invasion and migratory rate of 4T1 cells significantly reduced to 0.396 and 0.401, respectively. This demonstrated that the migratory and invasion of highly metastatic 4T1 tumor cells could be effectively suppressed after HA-BP reversed TAMs phenotype. In general, the above results indicated that the HA-BP exhibited great potential in suppressing the migration and metastasis of 4T1 cells.
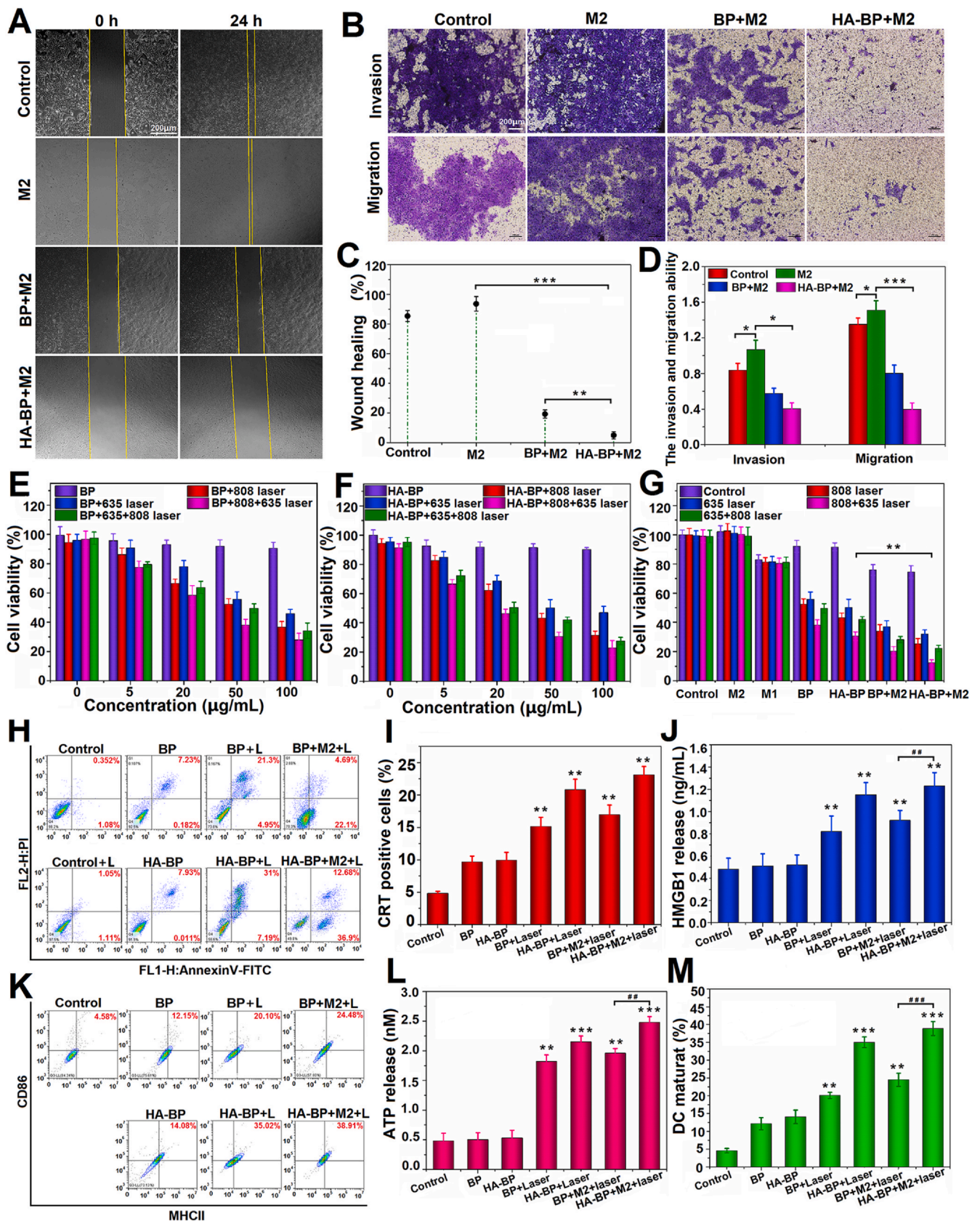
(caption on next page)

3.8. In vitro cytotoxicity

MTT assays were conducted to evaluate the cytotoxicity of BP and

HA-BP nanoparticles on 4T1 cells. As revealed in Fig. 5E and F, there was no obvious cytotoxicity of BP and HA-BP on 4T1 cells even at the BP concentration up to 100 μg/mL without laser irradiation (cell

Fig. 5. (**A**) The images of wound healing at 0 h and 24 h. (**B**) Transwell invasion and migration assay of 4T1 cells treated with various formulations. (**C**) The wound healing ratio of 4T1 cells with different treatments at 24 h. (**D**) The invasion and migration results of 4T1 cells treated with various formulations. (**E-G**) 4T1 cell viability of varying formulations with or without 808 nm (1.5 W/cm^2, 2 min) and 635 nm (0.5 W/cm^2, 5 min) laser irradiation. (**H**) Flow cytometry results of 4T1 cells apoptosis caused by different samples with or without 808 nm (1.5 W/cm^2, 2 min) and 635 nm (0.5 W/cm^2, 5 min) laser irradiation. (**I, J and L**) ICD signal molecules detections: (**I**) Flow cytometric analysis of CRT expression on the surface of 4T1 cells after treated with BP and HA-BP with or without laser irradiation. (**J**) HMGB1 detection in the supernatant. (**L**) ATP detection in the supernatant. (**K and M**) The expression of MHCII and CD86 of mature DCs induced by ICD signaling molecules. $*p < 0.05$, $**p < 0.01$ and $***p < 0.001$ as contrast with Control group, $^\#p < 0.05$, $^{\#\#}p < 0.01$ and $^{\#\#\#}p < 0.001$.

viability > 90%). Next, the phototherapy (PDT and PTT) effects of BP and HA-BP nanoparticles were investigated under 635 nm and 808 nm laser irradiation. Cell viability slightly decreased when exposed to 635 nm or 808 nm laser alone, and the cell viability of HA-BP with laser irradiation groups were all lower than that of BP with laser irradiation groups, which was attributed to enhanced cellular internalization of HA-BP than BP. To testify the combined effect of PTT and PDT, we measured the cytotoxicity of BP or HA-BP under the 808 + 635 nm laser and 635 + 808 nm laser, respectively. The final results displayed that both BP and HA-BP displayed stronger photo-induced cytotoxicity of 808 + 635 nm laser than that of 635 + 808 nm laser. Especially, the cells treated with HA-BP had a lower viability (30.5%) at the concentration of 50 μg/mL with 808 + 635 nm laser irradiation than that of HA-BP + 635 + 808 nm laser group (41.9%). The higher cytotoxicity of HA-BP could be attributed to stronger cellular internalization brought by HA modification under laser irradiation, and the higher cytotoxicity of HA-BP + 808 + 635 nm laser was explained that the hyperthermia by PTT resulted in more singlet oxygen and improved the effect of PDT. Besides, to further evaluate the cytotoxic effect of BP and HA-BP nanoparticles on tumor cell with macrophages polarization, M2 macrophages were treated with BP or HA-BP to collect relevant condition medium and the cytotoxicity of 4T1 cells was detected. As shown in Fig. 5G, the cytotoxicity was enhanced when 4T1 cells were exposed to the M1 condition medium but reduced in the M2 condition medium, indicating that M1 macrophages were efficient to sensitize 4T1 cells and had cytotoxicity on 4T1 cells to some degree. Meanwhile, both BP + M2 and HA-BP + M2 groups exhibited the enhanced anti-tumor efficacy with or without laser irradiation. The phenomenon was probably because that nanoparticles could induce M2 macrophages transformation into anti-tumor M1 macrophages, M1 macrophages could secret a series of pro-inflammatory cytokines (such as IL-6, IL-23 and IL-12), oxygen species (such as H$_2$O$_2$, superoxide) and reactive nitrogen (such as NO, iNOS) to prevent tumor cells proliferation [31,32]. Especially, cell viability sharply decreased to 12.3% in HA-BP + M2 + 808 + 635 nm laser group, which was on account of the combination of PTT-enhanced PDT and immunotherapy from M1 macrophages polarized from M2 macrophages by HA-BP nanoparticles. All above results suggested HA-BP can effectively kill tumor cells under 808 + 635 nm laser irradiation.

3.9. Cell apoptosis assay

The phototherapy of HA-BP and immunotherapy of M1 macrophages could induce cell apoptosis, which was detected via Annexin V-FITC/PI staining. As revealed in Fig. 5H, treatment with BP and HA-BP without NIR irradiation did not induce obvious apoptosis in comparison to Control group, and the cell apoptosis rates were 7.41% and 7.94%, respectively. However, when the cells were treated with laser irradiation, the cell apoptosis ratio of HA-BP treated with 4T1 cells was 38.2% (7.19% of early stage and 31% of late stage), higher than that of treatment with BP (26.3%), which could be attributed to HA capping that promoted more nanoparticles to enter the cells, and thus enhanced phototherapy to induce cell apoptosis. Importantly, the apoptosis rate of cells treated with HA-BP + M2 under 808 + 635 nm laser irradiation was 49.6% (36.9% of early stage and 12.68% of late stage), which was far higher than that of BP + M2 group (26.8%), indicating that HA-BP can reverse pro-tumor M2 macrophages to anti-tumor M1 macrophages,

which dramatically enhanced phototherapy-induced cell apoptosis, majorly in early stage. The above results illustrated that HA-BP nanoparticles is an excellent phototherapy agent to inhibit cells proliferation and significantly enhance cell apoptosis with M1 macrophages.

3.10. In vitro ICD evaluation

In general, when triggered cell death by specific factors, tumor cells without immunogenicity can be transformed into immunogenic cells, which activate the phagocytosis of immature DCs and lead to DC maturation ultimately. Mature DCs subsequently induce immune killing activity against the initial tumor cells in the host body, and this phenomenon is called ICD [43,44]. It has been identified that ICD inducers included certain chemotherapeutics, ionizing radiation, PTT and PDT [54–56]. The exposure of DAMPs (containing CRT, ATP and HMGB1) is prerequisite for DC maturation to trigger ICD-mediated antitumor immunity, so we evaluated the expression and release of the DAMPs of various treatments. As shown in Fig. 5I, BP and HA-BP nanoparticles without laser irradiation had little influence on CRT exposure. HA-BP + L (808 + 635 nm laser) with and without M2 condition medium treatment both exhibited the strongest increase in CRT expression compared with BP + L group. Especially, the CRT-exposure positive cells after HA-BP + M2 + L treatment was up to 23.1%, which was attributed to the phototherapy of HA-BP and anti-tumor effect of M1 macrophages. Besides, the results in Fig. 5J and L showed that HA-BP + M2 + L treatment group made for highest levels of HMGB1 release and ATP secretion compared among all treatment groups. These results indicated that combination of phototherapy and macrophages was a powerful strategy to improve DAMPs release and result in ICD. Moreover, DC maturation was also detected via the cell surface specific expression of MHCII and CD86 by flow cytometry. As shown in Fig. 5K and M, correspondingly, HA-BP + L (808 + 635 nm laser) group exhibited a significant enhancement of DC maturation compared with BP + L (808 + 635 nm laser) group, this was because that enhanced phototherapy effects of HA-BP induced stronger ICD effect than that of BP (Fig. 5I, J and L). Additionally, HA-BP + M2 + L (808 + 635 nm laser) induced the most incremental expression of both CD86 and MHCII on DCs among various treatment groups, indicating the optimal effect on the maturation of DCs. These results demonstrated that ROS, heating and macrophages are potent factors to induce ICD, which is essential to stimulate T lymphocyte-mediated adaptive immunity *in vivo*.

3.11. In vivo visual imaging

The performance of HA-BP nanoparticles for *in vivo* NIR optical fluorescence imaging was observed in 4T1 tumor-bearing mice (Fig. 6A and B). After intravenous (*i.v.*) injection of DIR, BP/DIR or HA-BP/DIR, the fluorescence signal of free DIR was distributed mainly in liver tissue and less in tumor within 48 h, exhibiting a poor tumor targeting specificity. For BP/DIR-treated mice, fluorescence signal in tumor regions was the strongest at 4 h post-administration and eliminated from the body gradually. Noticeably, HA-BP/DIR displayed stronger fluorescence intensity and had a relatively long duration (at least 48 h) in tumor tissue. Major accumulation was visible in tumor (reached maximum at 8 h) but not in liver or other tissues within 48 h post-administration. At 48 h post-injection, all mice were dissected and major organs were harvested. The fluorescence images and quantification of
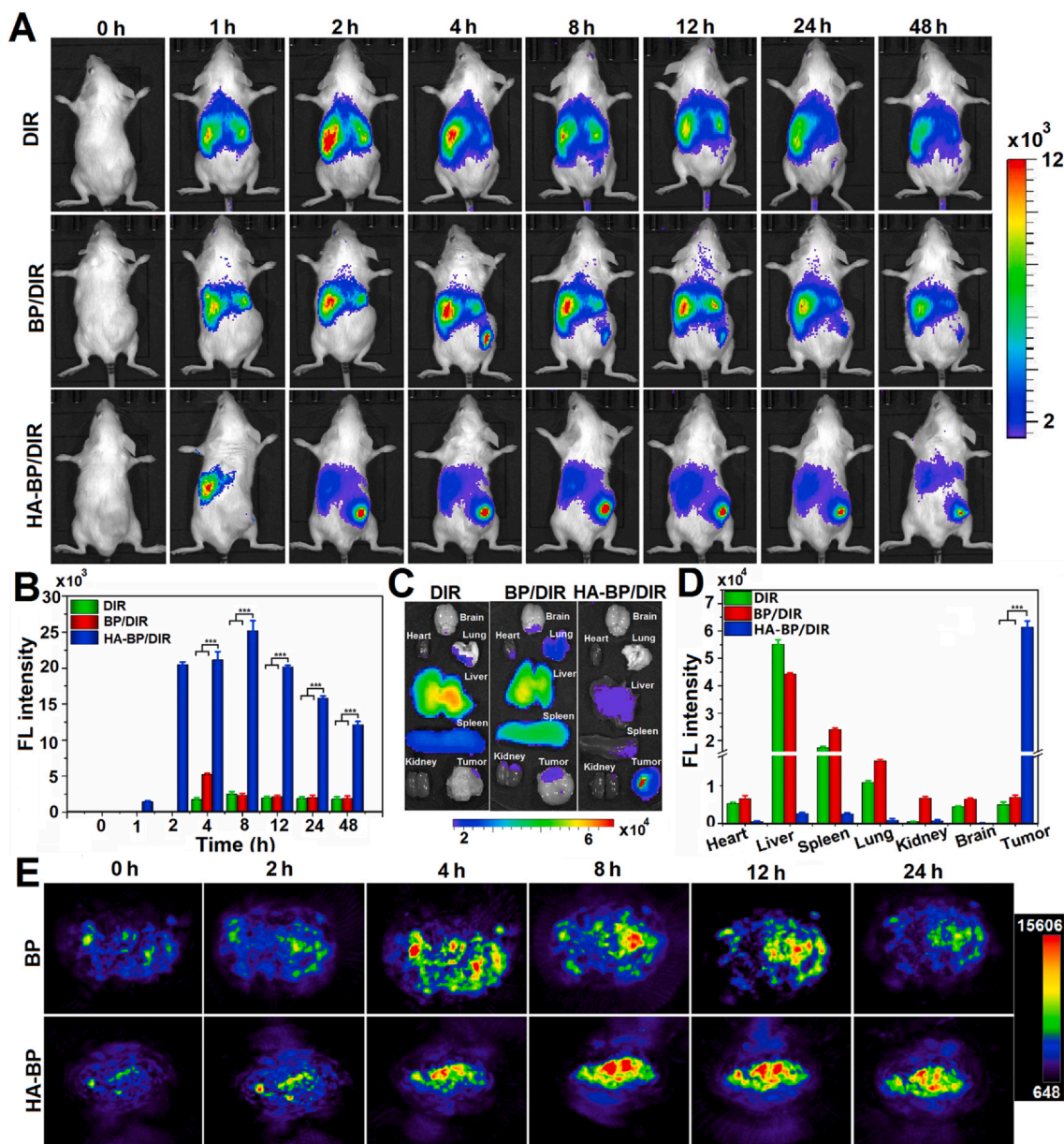
Fig. 6. (**A**) *In vivo* fluorescence imaging of 4T1 cancer-bearing mice after the injection of free DIR, BP/DIR and HA-BP/DIR foe different time intervals. (**B**) Semiquantitative fluorescence intensity statistics of tumor tissues at different time. (**C**) *Ex vivo* fluorescence imaging of major tissues at 48 h post injection. (**D**) The quantification of fluorescence intensity of various tissues. (**E**) PA signal images of 4T1 solid tumors at various time points after intravenously administration of BP and HA-BP nanoparticles, respectively. *$p < 0.05$, **$p < 0.01$ and ***$p < 0.001$.

major tissues were shown in Fig. 6C and D. In the DIR and BP/DIR groups, the DIR mostly accumulated in liver and spleen, while the fluorescence intensities of HA-BP/DIR group were 17.6 times and 24.6 times as high as that of BP/DIR and DIR groups, respectively. HA-BP/DIR significantly strengthened DIR accumulation in tumor tissue because of both CD44$^+$ targeting and EPR effect of the nanoplatform. To further validate the tumor imaging performance of HA-BP, PA signals of BP and HA-BP nanoparticles were monitored by tail vein injection as shown in Fig. 6E. PA signaling intensity of BP group enhanced gradually with time and reduced apparently at 12 h and 24 h, while PA signaling intensity of HA-BP group was up to the highest level in the surrounding of blood vessels at 8 h and considerable signal lasted for up to 24 h, achieving the real-time bioimaging. These results indicated that HA-BP nanoparticles exhibited notable dual-modal FL/PA imaging capacities and possessed an excellent tumor targeting ability.

3.12. In vivo anti-tumor therapy

Based on the test results *in vitro*, *in vivo* experiments were further carried out to investigate the tumor phototherapy efficacy of HA-BP nanoparticles on 4T1 cancer-bearing mice. As shown in Fig. 7A, 4T1 cells were inoculated into the mice, BP or HA-BP were intravenously injected for five times (1d, 3d, 5d, 7d and 9d), the mice of laser groups were exposed to 808 nm laser or 635 nm laser at 4 h after each injection, then the mice of all groups were executed and analyzed at the 21st day. The real-time temperature variation of tumor site was monitored by an infrared thermal camera (Fig. 7B). It was noticeable that the temperature in tumor site rapidly rose from 36.4 °C to 53.6 °C under 808 nm laser irradiation within 3 min after *i.v.* injection of HA-BP nanoparticles, a condition sufficient to ablate the malignant tumor, while the PBS and BP injected mice only exhibited slight increase of temperature. The phototherapy and immunotherapy efficiencies of HA-BP
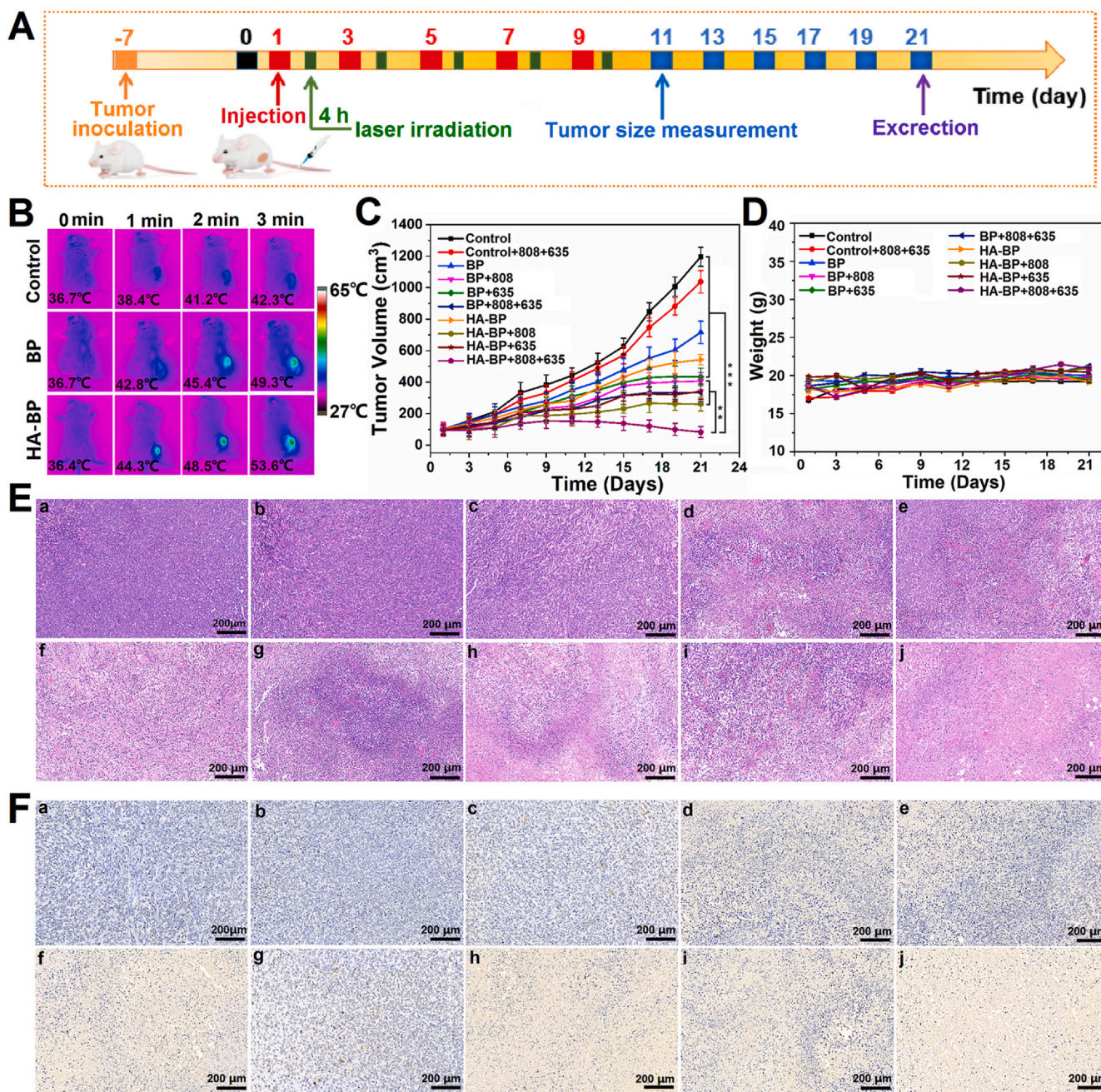
Fig. 7. *In vivo* therapeutic efficiency in 4T1 cancer-bearing mice **(A)** Schematic illustration of tumor model establishment and therapy process of HA-BP. **(B)** The temperature images of 4T1 cancer-bearing mice exposed to 808 nm laser within 3 min. **(C)** The variation of tumor volume with different treatments. **(D)** Variations of body weight scaled during various treatments. **(E)** H&E staining of tumor tissues dissected from the mice in various groups (a: Control; b: Control + 808 + 635 nm laser; c: BP; d: BP + 808 nm laser; e: BP + 635 nm laser; f: BP + 808 + 635 nm laser; g: HA-BP; h: HA-BP + 808 nm laser; i: HA-BP + 635 nm laser; j: HA-BP + 808 + 635 nm laser). **(F)** TUNEL immunohistochemical staining results of tumor tissues in different groups (a: Control; b: Control + 808 + 635 nm laser; c: BP; d: BP + 808 nm laser; e: BP + 635 nm laser; f: BP + 808 + 635 nm laser; g: HA-BP; h: HA-BP + 808 nm laser; i: HA-BP + 635 nm laser; j: HA-BP + 808 + 635 nm laser). $*p < 0.05$, $**p < 0.01$ and $***p < 0.001$.

were further investigated *in vivo*. Fig. 7C showed the change of tumor volume over time, the visual images of tumor tissues were shown in Fig. S10. Tumors in the Control and Control + 808 + 635 nm laser groups grew quickly, indicating the negligible influence of NIR laser irradiation on tumor growth rate. Treatments with HA-BP nanoparticles without laser irradiation only slightly inhibited tumor growth, which might be attributed to the anti-tumor effect of M1 macrophages re-educated by HA-BP nanoparticles. The tumor growth was partially suppressed in BP nanoparticles with single or double laser groups and HA-BP nanoparticles with single laser groups, and the anti-tumor effect of HA-BP

with 808 nm laser groups were better than that of HA-BP + 635 nm laser groups, indicating that PTT effect of HA-BP nanoparticles was more effective to inhibit tumor growth than PDT effect. In comparison, combined PDT/PTT/immunotherapy of HA-BP nanoparticles triggered by double laser irradiation significantly inhibited tumor growth, achieving noteworthy tumor regression with a tumor volume of 83.01 mm³. This result indicated that HA-BP nanoparticles combined with 808 + 635 nm laser exhibited a valid anti-tumor effect. H&E staining results of tumor tissues were shown in Fig. 7E. The tumor cells of Control and Control + 808 + 635 nm laser groups were integrated and

closely arranged without tumor fragmentation, while various degrees of karyolysis, piecemeal necrosis and fragmentation were observed in other treatment groups. Expectedly, symptoms containing karyotheca lysis, severe necrosis and nucleolus vanishing were most noticeable in the HA-BP + 808 + 635 nm laser group, and there were almost no apparent live tumor cells, exhibiting considerable therapeutic effect. Besides, the mice in HA-BP + laser groups survived for over 21 days without a death until they were executed, while half of the mice in the control group died or exceeded the established end-value 1200 mm^3 after treatment for 15 days (Fig. S11), indicating HA-BP plus laser irradiation could effectively prolonged the survival time of the mice. Therefore, it is mentioned that HA-BP nanoparticles could be as a promising agent for phototherapy and immunotherapy in the clinical trials in the future.

For further applications of the nanomaterials, their latent short-term toxicities *in vivo* were supposed to be particularly concerned. Over 21 days of treatment, the body weights of all mouse groups showed no noticeable loss and remained a slight upward trend (Fig. 7D). Besides, the H&E staining images (Fig. S12) of major tissues in all groups did not exhibit any obvious abnormality, demonstrating that the nanomaterials were relatively safe for application. Additionally, serum biochemistry assay of indicators (including AST, ALT, ALB, ALP, γ-GT, BUN and CRE, which are all relative to the functions of liver or kidney) were performed to determine the long-term toxicity *in vivo*. As shown in Fig. S13, the biochemistry results in BP and HA-BP groups were similar with those of Control group, and all indicators were in the normal reference range, manifesting that there were no obvious side effects on liver and kidney caused by BP and HA-BP nanoparticles.

3.13. Immunohistochemistry and immunofluorescence

TUNEL staining can precisely indicate DNA fracture induced by apoptosis instead of necrosis of cells so that the result would not be influenced by non-apoptosis caused by external radiation like laser. As shown in Figs. 7F and S14, almost no apoptotic cells were observed in Control and Control + 808 + 635 nm laser groups, and the nuclei of tumor cells had an intact shape. In the BP, BP + 808 nm, BP + 635 nm laser and HA-BP groups, there were small amounts of apoptotic cells (brown granules). However, a great amount of abnormal tumor cells was observed in HA-BP + 808 nm, HA-BP + 635 nm and HA-BP + 808 + 635 nm laser groups. More importantly, most of tumor cells became dark brown granular nuclei in the HA-BP + 808 + 635 nm laser groups, which was consistent with H&E staining results, indicating that HA-BP could significantly cause apoptosis of tumor cells.

Furthermore, to further investigate the therapeutic effects of HA-BP nanoparticles, the polarization of TAMs, factors including Ki67, MMP-9 and CD31 that were correlated with tumor proliferation and metastasis were assessed via immunofluorescence staining. As revealed in Fig. 8A and B, the percentages of M2 macrophages in HA-BP and HA-BP + L (808 + 635 nm laser) groups were obviously lower than that in Control and Control + L groups, while the percentages of anti-tumor M1 macrophages in HA-BP and HA-BP + L groups significantly increased. These results were consistent with results *in vitro*, proving that HA-BP successfully polarized pro-tumor M2 macrophages to pro-inflammatory and anti-tumor M1 macrophages. Besides, as a matrix metalloproteinase produced by macrophages, MMP-9 is expressed responding to the stimulation of tumorigenic factors, and the tumor cells of preliminary regions could cause the expression of MMP-9 and Ki67 [57]. As shown in Fig. 8A, C and D, in comparison with Control and Control + L (808 + 635 nm laser) groups, the expression of MMP-9 and Ki67 significantly decreased in BP and HA-BP groups, and almost no the expression of MMP-9 and Ki67 was observed in HA-BP + L (808 + 635 nm laser) group, implying the reduced metastasis and proliferation activities of tumor cells caused by BP and HA-BP nanoparticles. Besides, matrix metalloproteinase is proved to be directly involved in angiogenesis and invasion [58]. So we further explored the expression of

CD31, a marker of vascular endothelial and indicator of angiogenesis at the tumor sites, the results were shown in Fig. 8A and E. The expression of CD31 in BP + L (808 + 635 nm laser) groups declined dramatically, and HA-BP + L (808 + 635 nm laser) group showed the lowest expression of CD31 among all treatment groups, which was attributed to the phototherapy effect and a decrease in the number of M2 macrophages. According to the valid effect of BP-based phototherapy on DAMPs release *in vitro*, CRT exposure in tumor sites after treatment was measured as a typical biomarker of ICD. As revealed in Fig. 8A and F, Control and Control + L (808 + 635 nm laser) groups hardly induced CRT exposure because of few green fluorescence (anti-CRT antibodies) in tumor tissues, and BP or HA-BP alone exhibited a small amount of CRT exposure. However, enhanced fluorescence intensity was shown in BP + L (808 + 635 nm laser) group and the brightest green fluorescence appeared in HA- BP + L (808 + 635 nm laser) group, indicating that BP and HA-BP had a potent ICD-inducing effect under NIR laser irradiation *in vivo*. In addition, the infiltration of immune cells into tumor sites is essential for the tumor immunotherapy, so the recruitment of CD4$^+$ and CD8$^+$ T lymphocytes by the anti-tumor effect of HA-BP mediated phototherapy was evaluated. As shown in Fig. 8A and G, there were almost no CD4$^+$ (red fluorescence) and CD8$^+$ (green fluorescence) cells observed in Control, Control + L (808 + 635 nm laser) groups, and BP or HA-BP groups showed a small amount of CD4$^+$ and CD8$^+$ T cells in the tumor sites, which might be because that BP or HA-BP induced the pro-tumor M2 macrophages to pro-inflammatory and anti-tumor M1 macrophages, M1 macrophages could secret a series of pro-inflammatory cytokines (such as IL-6, IL-23 and IL-12) to alleviate immunosuppressive microenvironment and activate T cell immune response [28]. In contrast, BP + L (808 + 635 nm laser) and HA-BP + L (808 + 635 nm laser) groups exhibited a significantly stronger infiltration CD4$^+$ and CD8$^+$ T cells, implying that CD4$^+$ and CD8$^+$ T cell-dependent anti-tumor immunity was induced by phototherapy. Importantly, HA-BP + L displayed the highest proportion of CD4$^+$ and CD8$^+$ T cells owing to the stronger phototherapy effects and alleviation of immunosuppressive microenvironment from M1 macrophages. All of the results demonstrated that HA-BP exhibited excellent phototherapy efficiency and could induce a robust anti-tumor immune response.

4. Conclusion

In this study, HA-BP nanoparticles were successfully prepared as a macrophage converter and tumor-targeted photosensitizer to achieve tumor photo-immunotherapy. *In vitro* and *in vivo* results manifested that HA-BP nanoparticles could obviously reduce the degradation of BP and improve the stability. Meanwhile, HA-BP nanoparticles displayed excellent PA imaging ability and photothermal/photodynamic therapeutic efficiency under NIR irradiation, achieving effectively apoptosis of 4T1 cells. Importantly, HA-BP could promote the macrophage polarization from M2 to M1 phenotype and thus induce immunogenic cell death by phototherapy, resulting in increased proportion of DC maturation and enhanced invasion of activated CD4$^+$ and CD8$^+$ T cells in the tumor tissues, which significantly prevent malignant tumor proliferation without any apparent side reactions. In conclusion, this work offers a novel and safe strategy that achieves the combination therapy of phototherapy and immune-activation using BP nanoparticles.

CRediT authorship contribution statement

Xiaoge Zhang: Conceptualization, Methodology, Formal analysis, Data curation, Writing - original draft, Writing - review & editing. **Junjie Tang:** Investigation, Writing - review & editing. **Chao Li:** Investigation, Methodology. **Yao Lu:** Investigation, Writing - review & editing. **Lili Cheng:** Investigation. **Jie Liu:** Resources, Supervision, Writing - review & editing, Project administration, Funding acquisition.
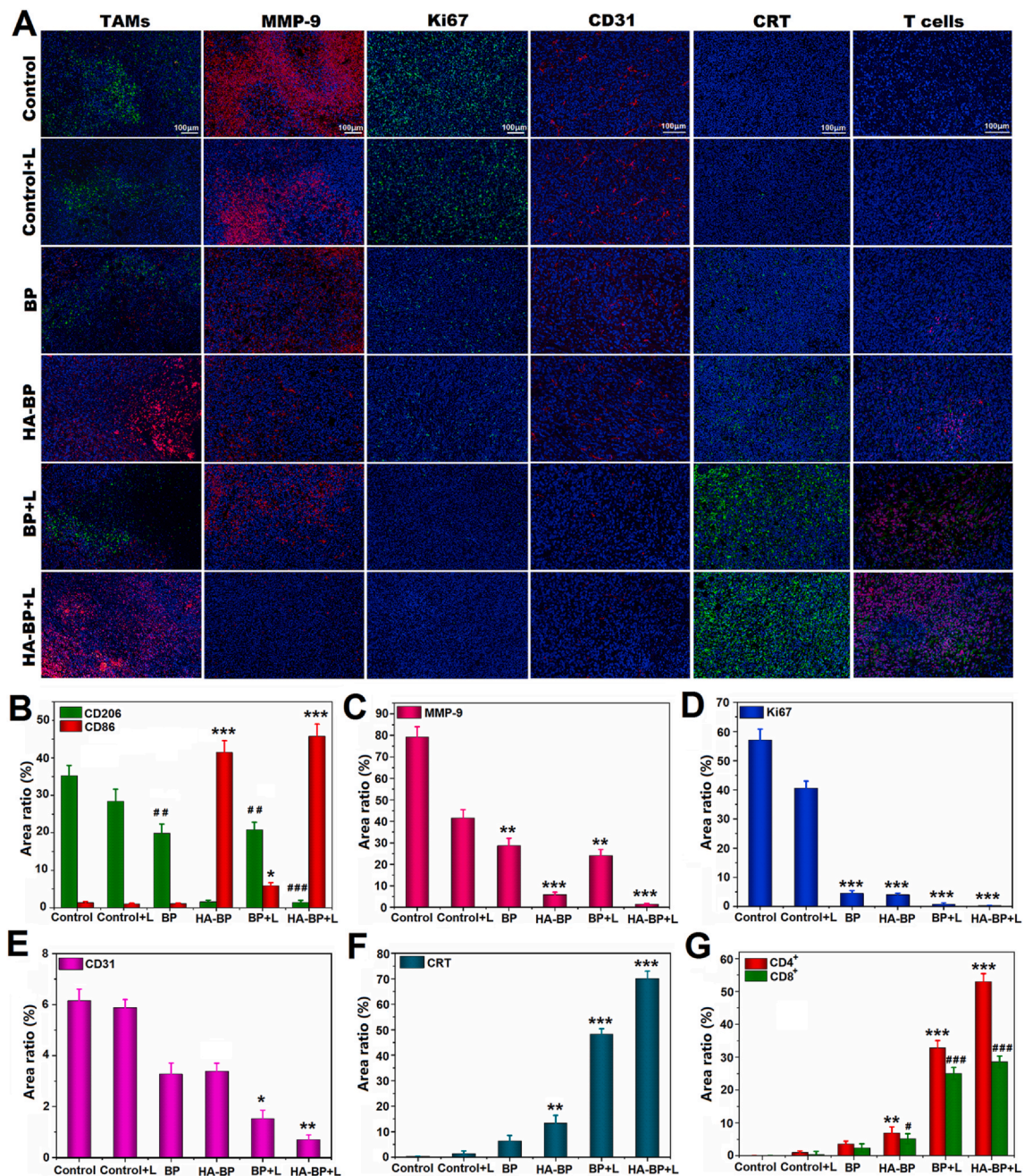
Fig. 8. (A) Representative immunofluorescence images of tumor tissues stained by TAMs (M2/CD206 (green), M1/CD86 (red)), MMP-9, Ki67, CD31 and T cells ($CD4^+$ (red) and $CD8^+$ (green)) in different groups with or without 808 + 635 nm laser. (B) The quantitative fluorescence area ratio of M1 and M2 (C) The quantitative fluorescence area ratio of MMP-9. (D) The quantitative fluorescence area ratio of Ki67. (E) The quantitative fluorescence area ratio of CD31. (F) The quantitative fluorescence area ratio of CRT. (G) The quantitative fluorescence area ratio of $CD4^+$ and $CD8^+$ T cells. *$p < 0.05$, **$p < 0.01$ and ***$p < 0.001$ as contrast with relevant Control group. (For interpretation of the references to color in this figure legend, the reader is referred to the Web version of this article.)

Declaration of competing interest

The authors declare that they have no known competing financial interests or personal relationships that could have appeared to influence the work reported in this paper.

Appendix A. Supplementary data

Supplementary data to this article can be found online at https://doi.org/10.1016/j.bioactmat.2020.08.024.

References

[1] Y. Hao, Y. Chen, X. He, F. Yang, R. Han, C. Yang, W. Li, Z. Qian, Near-infrared responsive 5-fluorouracil and indocyanine green loaded MPEG-PCL nanoparticle integrated with dissolvable microneedle for skin cancer therapy, Bioact Mater 5 (3) (2020) 542–552.

[2] S. Shi, R. Vissapragada, J. Abi Jaoude, C. Huang, A. Mittal, E. Liu, J. Zhong, V. Kumar, Evolving role of biomaterials in diagnostic and therapeutic radiation oncology, Bioact Mater 5 (2) (2020) 233–240.

[3] J.L. Arias, Drug targeting strategies in cancer treatment: an overview, Mini Rev. Med. Chem. 11 (1) (2011) 1–17.

[4] K. Dong, Z. Liu, Z. Li, J. Ren, X. Qu, Hydrophobic anticancer drug delivery by a 980 nm laser-driven photothermal vehicle for efficient synergistic therapy of cancer cells in vivo, Adv. Mater. 25 (32) (2013) 4452–4458.

[5] T. Qi, B. Chen, Z. Wang, H. Du, D. Liu, Q. Yin, B. Liu, Q. Zhang, Y. Wang, A pH-Activatable nanoparticle for dual-stage precisely mitochondria-targeted photodynamic anticancer therapy, Biomaterials 213 (2019) 119219.

[6] X. Li, C. Zhang, Q. Zheng, X. Shi, ROS-responsive targeting micelles for optical imaging-guided chemo-phototherapy of cancer, Colloids Surf. B Biointerfaces 179 (2019) 218–225.

[7] Y.R. Cheng, F. Yang, K. Zhang, Y.Y. Zhang, Y. Cao, C.H. Liu, H.T. Lu, H.F. Dong, X.J. Zhang, Non-fenton-type hydroxyl radical generation and photothermal effect by mitochondria-targeted WSSe/MnO2 nanocomposite loaded with isoniazid for synergistic anticancer treatment, Adv. Funct. Mater. 29 (45) (2019).

[8] L.Z. Feng, Z.L. Dong, D.L. Tao, Y.C. Zhang, Z. Liu, The acidic tumor micro-environment: a target for smart cancer nano-theranostics, Natl Sci Rev 5 (2) (2018) 269–286.

[9] Z.H. Lu, S.J. Liu, Y.G. Le, Z.N. Qin, M.W. He, F.B. Xu, Y. Zhu, J.M. Zhao, C.B. Mao, L. Zheng, An injectable collagen-genipin-carbon dot hydrogel combined with photodynamic therapy to enhance chondrogenesis, 218 Biomaterials, 2019119190233 (2020).

[10] J.J. Qiu, Q.F. Xiao, X.P. Zheng, L.B. Zhang, H.Y. Xing, D.L. Ni, Y.Y. Liu, S.J. Zhang, Q.G. Ren, Y.Q. Hua, K.L. Zhao, W.B. Bu, Single W18O49 nanowires: a multi-functional nanoplatform for computed tomography imaging and photothermal/ photodynamic/radiation synergistic cancer therapy, Nano Res 8 (11) (2015) 3580–3590.

[11] H. Wang, X. Pan, X. Wang, W. Wang, Z. Huang, K. Gu, S. Liu, F. Zhang, H. Shen, Q. Yuan, J. Ma, W. Yuan, H. Liu, Degradable carbon-silica nanocomposite with immunoadjuvant property for dual-modality photothermal/photodynamic therapy, ACS Nano 14 (3) (2020) 2847–2859.

[12] J. Xu, L. Xu, C. Wang, R. Yang, Q. Zhuang, X. Han, Z. Dong, W. Zhu, R. Peng, Z. Liu, Near-infrared-triggered photodynamic therapy with multitasking upconversion nanoparticles in combination with checkpoint blockade for immunotherapy of colorectal cancer, ACS Nano 11 (5) (2017) 4463–4474.

[13] R. Liang, L. Liu, H. He, Z. Chen, Z. Han, Z. Luo, Z. Wu, M. Zheng, Y. Ma, L. Cai, Oxygen-boosted immunogenic photodynamic therapy with gold nanocages@manganese dioxide to inhibit tumor growth and metastases, Biomaterials 177 (2018) 149–160.

[14] S. Hameed, S. Mo, G. Mustafa, S.Z. Bajwa, W.S. Khan andZ. Dai, Immunological consequences of nanoparticle-mediated antitumor photoimmunotherapy, Adv. Ther 3 (5) (2019) 1900101.

[15] B. Xing, L. Guan, Y. Yu, X. Niu, X. Yan, S. Zhang, J. Yao, D. Wang, J. Sha, Y. Wang, HfO2-passivated black phosphorus field effect transistor with long-termed stability and enhanced current on/off ratio, Nanotechnology 30 (34) (2019) 345208.

[16] H. Liu, Y. Du, Y. Deng, P.D. Ye, Semiconducting black phosphorus: synthesis, transport properties and electronic applications, Chem. Soc. Rev. 44 (9) (2015) 2732–2743.

[17] B. Li, C. Lai, G. Zeng, D. Huang, L. Qin, M. Zhang, M. Cheng, X. Liu, H. Yi, C. Zhou, F. Huang, S. Liu, Y. Fu, Black phosphorus, a rising star 2D nanomaterial in the post-graphene era: synthesis, properties, modifications, and photocatalysis applications, Small 15 (8) (2019) e1804565.

[18] F. Xia, H. Wang, Y. Jia, Rediscovering black phosphorus as an anisotropic layered material for optoelectronics and electronics, Nat. Commun. 5 (2014) 4458.

[19] Z. Sun, H. Xie, S. Tang, X.F. Yu, Z. Guo, J. Shao, H. Zhang, H. Huang, H. Wang, P.K. Chu, Ultrasmall black phosphorus quantum dots: synthesis and use as photo-thermal agents, Angew Chem. Int. Ed. Engl. 54 (39) (2015) 11526–11530.

[20] C. Sun, L. Wen, J. Zeng, Y. Wang, Q. Sun, L. Deng, C. Zhao, Z. Li, One-pot sol-ventless preparation of PEGylated black phosphorus nanoparticles for photo-acoustic imaging and photothermal therapy of cancer, Biomaterials 91 (2016) 81–89.

[21] X. Yang, D. Wang, Y. Shi, J. Zou, Q. Zhao, Q. Zhang, W. Huang, J. Shao, X. Xie, X. Dong, Black phosphorus nanosheets immobilizing Ce6 for imaging-guided photothermal/photodynamic cancer therapy, ACS Appl. Mater. Interfaces 10 (15) (2018) 12431–12440.

[22] L. Tan, J. Li, X. Liu, Z. Cui, X. Yang, K.W.K. Yeung, H. Pan, Y. Zheng, X. Wang, S. Wu, In situ disinfection through photoinspired radical oxygen species storage and thermal-triggered release from black phosphorous with strengthened chemical stability, Small 14 (9) (2018).

[23] J. Zhou, Z. Li, M. Ying, M. Liu, X. Wang, X. Wang, L. Cao, H. Zhang, G. Xu, Black phosphorus nanosheets for rapid microRNA detection, Nanoscale 10 (11) (2018) 5060–5064.

[24] J. Liu, P. Du, T. Liu, B.J. Cordova Wong, W. Wang, H. Ju, J. Lei, A black phos-phorus/manganese dioxide nanoplatform: oxygen self-supply monitoring, photo-dynamic therapy enhancement and feedback, Biomaterials 192 (2019) 179–188.

[25] H. Huang, L. He, W. Zhou, G. Qu, J. Wang, N. Yang, J. Gao, T. Chen, P.K. Chu, X.F. Yu, Stable black phosphorus/Bi2O3 heterostructures for synergistic cancer radiotherapy, Biomaterials 171 (2018) 12–22.

[26] M. Qiu, D. Wang, W. Liang, L. Liu, Y. Zhang, X. Chen, D.K. Sang, C. Xing, Z. Li, B. Dong, F. Xing, D. Fan, S. Bao, H. Zhang, Y. Cao, Novel concept of the smart NIR-light-controlled drug release of black phosphorus nanostructure for cancer therapy, Proc. Natl. Acad. Sci. U. S. A. 115 (3) (2018) 501–506.

[27] J.P. Almeida, A.L. Chen, A. Foster, R. Drezek, In Vivo biodistribution of

[28] nanoparticles, Nanomedicine 6 (5) (2011) 815–835.

[28] H.S. Choi, J.V. Frangioni, Nanoparticles for biomedical imaging: fundamentals of clinical translation, Mol. Imag. 9 (6) (2010) 291–310.

[29] X. Zhong, B. Chen, Z. Yang, The role of tumor-associated macrophages in colorectal carcinoma progression, Cell. Physiol. Biochem. 45 (1) (2018) 356–365.

[30] S.K. Jeong, J.S. Kim, C.G. Lee, Y.S. Park, S.D. Kim, S.O. Yoon, D.H. Han, K.Y. Lee, M.H. Jeong, W.S. Jo, Tumor associated macrophages provide the survival resistance of tumor cells to hypoxic microenvironmental condition through IL-6 receptor-mediated signals, Immunobiology 222 (1) (2017) 55–65.

[31] N.T. Trac, E.J. Chung, Peptide-based targeting of immunosuppressive cells in cancer, Bioact Mater 5 (1) (2020) 92–101.

[32] V. Gupta, F. Yull, D. Khabele, Bipolar tumor-associated macrophages in ovarian cancer as targets for therapy, Cancers 10 (10) (2018).

[33] C.E. Lewis, J.W. Pollard, Distinct role of macrophages in different tumor micro-environments, Canc. Res. 66 (2) (2006) 605–612.

[34] S. Zanganeh, G. Hutter, R. Spitler, O. Lenkov, M. Mahmoudi, A. Shaw, J.S. Pajarinen, H. Nejadnik, S. Goodman, M. Moseley, L.M. Coussens, H.E. Daldrup-Link, Iron oxide nanoparticles inhibit tumour growth by inducing pro-inflammatory macrophage polarization in tumour tissues, Nat. Nanotechnol. 11 (11) (2016) 986–994.

[35] H. Zhang, X. Zhang, Y. Ren, F. Cao, L. Hou, Z. Zhang, An in situ microenvironmental nano-regulator to inhibit the proliferation and metastasis of 4T1 tumor, Theranostics 9 (12) (2019) 3580–3594.

[36] H. Peng, B. Chen, W. Huang, Y. Tang, Y. Jiang, W. Zhang, Y. Huang, (2020), Reprogramming tumor-associated macrophages to reverse EGFR(T790M) resistance by dual-targeting codelivery of gefitinib/vorinostat, Nano Lett. 17 (12) (2017) 7684–7690.

[37] D. Chen, J. Xie, R. Fiskesund, W. Dong, X. Liang, J. Lv, X. Jin, J. Liu, S. Mo, T. Zhang, F. Cheng, Y. Zhou, H. Zhang, K. Tang, J. Ma, Y. Liu, B. Huang, Chloroquine modulates antitumor immune response by resetting tumor-associated macrophages toward M1 phenotype, Nat. Commun. 9 (1) (2018) 873.

[38] M.H. El-Dakdouki, D.C. Zhu, K. El-Boubbou, M. Kamat, J. Chen, W. Li, X. Huang, Development of multifunctional hyaluronan-coated nanoparticles for imaging and drug delivery to cancer cells, Biomacromolecules 13 (4) (2012) 1144–1151.

[39] B.P. Toole, Hyaluronan-CD44 interactions in cancer: paradoxes and possibilities, Clin. Canc. Res. 15 (24) (2009) 7462–7468.

[40] J.E. Rayahin, J.S. Buhrman, Y. Zhang, T.J. Koh, R.A. Gemeinhart, High and low molecular weight hyaluronic acid differentially influence macrophage activation, ACS Biomater. Sci. Eng. 1 (7) (2015) 481–493.

[41] D.B. Lyle, J.C. Breger, L.F. Baeva, J.C. Shallcross, C.N. Durfor, N.S. Wang, J.J. Langone, Low molecular weight hyaluronic acid effects on murine macrophage nitric oxide production, J. Biomed. Mater. Res. 94 (3) (2010) 893–904.

[42] M. Song, T. Liu, C. Shi, X. Zhang, X. Chen, Correction to bioconjugated manganese dioxide nanoparticles enhance chemotherapy response by priming tumor-asso-ciated macrophages toward M1-like phenotype and attenuating tumor hypoxia, ACS Nano 10 (3) (2016) 3872.

[43] D.V. Krysko, A.D. Garg, A. Kaczmarek, O. Krysko, P. Agostinis, P. Vandenabeele, Immunogenic cell death and DAMPs in cancer therapy, Nat. Rev. Canc. 12 (12) (2012) 860–875.

[44] G. Kroemer, L. Galluzzi, O. Kepp, L. Zitvogel, Immunogenic cell death in cancer therapy, Annu. Rev. Immunol. 31 (2013) 51–72.

[45] J.W. Tian, L. Ding, H.J. Xu, Z. Shen, H.X. Ju, L. Jia, L. Bao, J.S. Yu, Cell-specific and pH-activatable rubyrin-loaded nanoparticles for highly selective near-infrared photodynamic therapy against cancer, J. Am. Chem. Soc. 135 (50) (2013) 18850–18858.

[46] M. Zhang, Z.W. Cui, R.X. Song, B. Lv, Z.M. Tang, X.F. Meng, X.Y. Chen, X.P. Zheng, J.W. Zhang, Z.W. Yao, W.B. Bu, SnWO4-based nanohybrids with full energy transfer for largely enhanced photodynamic therapy and radiotherapy, Biomaterials 155 (2018) 135–144.

[47] H.X. Shi, W.C. Sun, C.B. Liu, G.Y. Gu, B. Ma, W.L. Si, N.N. Fu, Q. Zhang, W. Huang, X.C. Dong, Tumor-targeting, enzyme-activated nanoparticles for simultaneous cancer diagnosis and photodynamic therapy, J. Mater. Chem. B 4 (1) (2016) 113–120.

[48] W.S. Chen, J. Ouyang, H. Liu, M. Chen, K. Zeng, J.P. Sheng, Z.J. Liu, Y.J. Han, L.Q. Wang, J. Li, L. Deng, Y.N. Liu, S.J. Guo, Black phosphorus nanosheet-based drug delivery system for synergistic photodynamic/photothermal/chemotherapy of cancer, Adv. Mater. 29 (5) (2017).

[49] L.L. Zhou, L. Chen, X.C. Hu, Y.L. Lu, W.J. Liu, Y.T. Sun, T.M. Yao, C.Y. Dong, S. Shi, A Cu9S5 nanoparticle-based CpG delivery system for synergistic photothermal-, photodynamic- and immunotherapy, Commun Biol 3 (1) (2020).

[50] M. Kawai, K. Guth, K. Winnikes, C. Haist, J.C. Ruegg, The effect of inorganic phosphate on the ATP hydrolysis rate and the tension transients in chemically skinned rabbit psoas fibers, Pflügers Archiv 408 (1) (1987) 1–9.

[51] G.S. Di Marco, M. Hausberg, U. Hillebrand, P. Rustemeyer, W. Wittkowski, D. Lang, H. Pavenstadt, Increased inorganic phosphate induces human endothelial cell apoptosis in vitro, Am. J. Physiol. Ren. Physiol. 294 (6) (2008) F1381–F1387.

[52] A. Spina, L. Sapio, A. Esposito, F. Di Maiolo, L. Sorvillo, S. Naviglio, Inorganic phosphate as a novel signaling molecule with antiproliferative action in MDA-MB-231 breast cancer cells, Biores Open Access 2 (1) (2013) 47–54.

[53] J. Ouyang, C. Feng, X.Y. Ji, L. Li, H.K. Gutti, N.Y. Kim, D. Artzi, A. Xie, N. Kong, Y.N. Liu, G.J. Tearney, X.B. Sui, W. Tao, O.C. Farokhzad, 2D monoelemental ger-manene quantum dots: synthesis as robust photothermal agents for photonic cancer nanomedicine, Angew. Chem. Int. Ed. 58 (38) (2019) 13405–13410.

[54] W. Song, J. Kuang, C.X. Li, M. Zhang, D. Zheng, X. Zeng, C. Liu, X.Z. Zhang, Enhanced immunotherapy based on photodynamic therapy for both primary and lung metastasis tumor eradication, ACS Nano 12 (2) (2018) 1978–1989.

[55] Z. Meng, X. Zhou, J. Xu, X. Han, Z. Dong, H. Wang, Y. Zhang, J. She, L. Xu, C. Wang, Z. Liu, Light-triggered in situ gelation to enable robust photodynamic-immunotherapy by repeated stimulations, Adv. Mater. 31 (24) (2019) e1900927.

[56] K. Ni, T. Aung, S. Li, N. Fatuzzo, X. Liang, W. Lin, Nanoscale metal-organic framework mediates radical therapy to enhance cancer immunotherapy, Inside Chem. 5 (7) (2019) 1892–1913.

[57] T.L. Rogers, I. Holen, Tumour macrophages as potential targets of bisphosphonates,

J. Transl. Med. 9 (2011) 177.

[58] S. Zeynali-Moghaddam, M. Mohammadian, F. Kheradmand, A. Fathi-Azarbayjani, Y. Rasmi, O. Esna-Ashari, H. Malekinejad, A molecular basis for the synergy between 17allylamino17demethoxy geldanamycin with Capecitabine and Irinotecan in human colorectal cancer cells through VEFG and MMP-9 gene expression, Gene 684 (2019) 30–38.